TECHNISCHE
UNIVERSITÄT
WIEN
Vienna University of Technology

DISSERTATION

# Theoretical Investigations of the Hexagonal Boron Nitride Nanomeshes

ausgeführt zum Zwecke der Erlangung des akademischen Grades eines
Doktors der technischen Wissenschaften
unter der Leitung von

ao. Univ. Prof. Dipl.-Ing. Dr. Peter Blaha
E165
Institut für Materialchemie

eingereicht an der Technischen Universität Wien
Fakultät für Technische Chemie

von
Dipl.-Ing. Thomas Gallauner
9725143
Gerasdorferstraße 55/9/3
A-1210 Wien

Wien, den 4. Februar 2011 Thomas Gallauner

# Contents

# Part I

# Preface

# Acknowledgment


- *Ao. Univ.-Prof. Dr. Peter Blaha* and *Univ.-Prof. Dr. Karlheinz Schwarz* for giving me the possibility to carry out this thesis and their continuous support.
- *Dr. Robert Laskowski* for his support and the preliminary work on which much of this thesis is based on.
- The *EU* for funding the nanomesh project.
- The *Aurora project* for partly funding this project and providing the computational resources.

# Abstract

This thesis deals with the theoretical investigation and characterization of systems formed by hexagonal boron nitride on top of the (111) surfaces of nickel, rhodium and platinum.

The *h*-BN/Ni(111) system was studied to carry out simulations of NEXAFS spectra for the B-K and N-K edge and to investigate the bonding properties in detail.

The *h*-BN/Rh(111) and *h*-BN/Pt(111) systems form a selfassembled structure called *nanomesh* and are investigated using the software package OpenMX, which is an order-N DFT method that is less demanding than other schemes with respect to computational resources. The results obtained are compared with both experimental data and results calculated with WIEN2k.

In the last part of this work a possible reaction path for the formation of the *h*-BN layer on the Rh(111) surface is studied by theory.

# Kurzfassung der Arbeit

Diese Arbeit beschäftigt sich mit der theoretischen Untersuchung von Oberflächensystemen, die auf der Bildung einer Monolage hexagonalen Bornitrides auf den (111)-Oberflächen von Nickel, Rhodium und Platin basiert.

Für das *h*-BN/Ni(111)-System wurden sowohl NEXAFS-Spektren für die B-K und N-K Absorptionskanten simuliert, als auch die genaue elektronische Struktur zur detaillierten Aufklärung der Bindungseigenschaften berechnet.

Die Bildung von hexagonalem Bornitrid auf Rhodium und Platin führt zu selbstgeordneten regelmäßigen Strukturen (genannt *Nanomesh*), welche eine sehr große Einheitszelle aufweisen und daher mit der Software OpenMX untersucht wurden, da diese DFT Berechnungen ermöglicht hat, welche nur linear mit der Anzahl der Atome skalieren. Die erhaltenen Ergebnisse wurden mit experimentellen Daten sowie Berechnungen mit dem Programm WIEN2k verglichen.

Im dritten Teil wird aufgrund theoretischer Überlegungen ein möglicher Reaktionsweg entwickelt, welcher die Bildung von hexagonalem Bornitrid aus Borazin auf der Rh(111)-Oberfläche beschreibt.

# Part II

# Research Objectives

This thesis focuses on the theoretical characterization and investigation of surface systems consisting of *h*-BN formed on metal surfaces with (111) orientation and the study of a possible reaction path that describes how these systems are formed.

The following steps were carried out:

- The detailed characterization of the *h*-BN/Ni(111) system, especially
  - a simulation of the NEXAFS spectra for the B-K and N-K absorption edge and the
  - investigation of bonding properties between the metal substrate and the *h*-BN layer using the WIEN2k software.
- An investigation of the possibility and accuracy of the geometry optimization with OpenMX (an order-N DFT software) for the single layer models of
  - *h*-BN on Rh(111) and
  - *h*-BN on Pt(111) with
  - Comparison of the obtained results with both experiment and WIEN2k calculations.
- A theoretical investigation of a possible reaction path for the formation of *h*-BN on Rh(111).

# Part III

# Introduction

# Chapter 1

# Boron Nitride Nanomesh on Rh(111)

## 1.1 Discovery

The formation of hexagonal boron nitride ($h$-BN) layers on metal surfaces gained increasing attention in recent years. Hexagonal boron nitride is isostructural and isoelectronic to graphite and thus has many similar properties. However, in contrast to the carbon-carbon bonding, with the well known delocalized $\pi$ electron system, boron and nitrogen have a different electronegativity resulting in a partial ionic bonding forming an insulator. Besides the interest in basic research those well ordered layer structures on metal surfaces may offer a manifold of technical applications. Some of these structures like the $h$-BN/Ni(111) are already well investigated by experiment [2, 3] and theory [4]. In the case of Ni(111) the interface metal layer has nearly the same in-plane lattice parameter as a simple $h$-BN layer and thus a well defined epitaxial structure is formed. In 2004 a completely different type of system was found when boron nitride was depostied on a Rh(111)

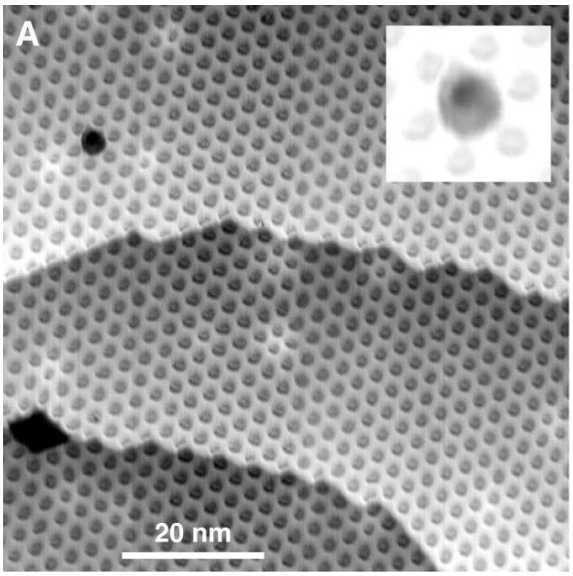


Figure 1.1: STM image of the *h*-BN nanomesh on Rh(111) [5]

surface [5]. First investigations using scanning tunneling microscopy (STM) did not show the expected homogenous epitaxial surface, but a pattern of a honeycomb like structure, as can be seen in figure 1.1. The structure is well ordered but shows a periodicity of approximately 3.2 nm, which was called 'nanomesh'. This completely different behavior of *h*-BN on the rhodium surface comes most likely from the large lattice mismatch between Rh(111) and *h*-BN of 6.7 percent, which would lead to a highly strained structure when epitaxially grown. In contrast to rhodium the mismatch for *h*-BN/Ni(111) is only 0.4 percent.

## 1.2 Synthesis

The *h*-BN nanomesh was prepared [5] by exposing the clean Rh(111) surface to borazine vapor at a temperature of 1070 K. The reaction was carried out

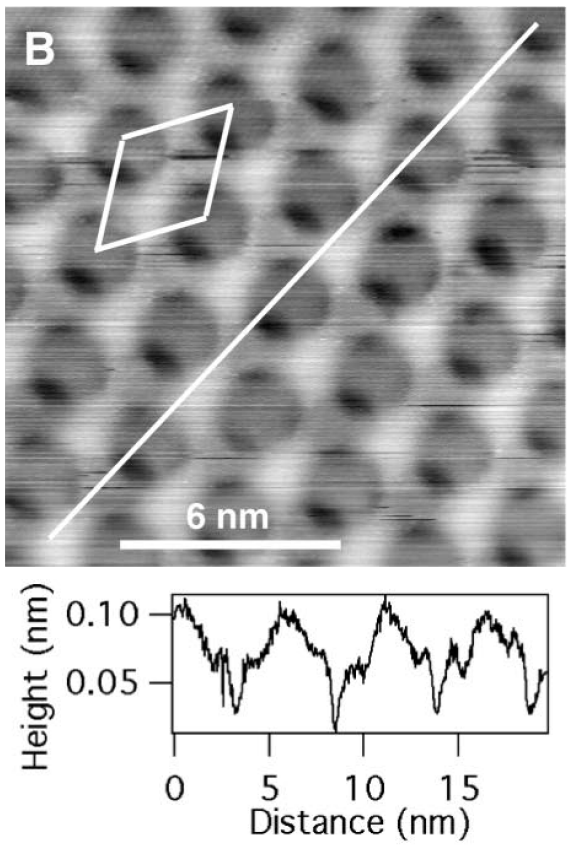


Figure 1.2: STM image of the $h$-BN nanomes on Rh(111) with higher resolution and height profile along the line [5].

in an ultrahigh vacuum chamber with a vapor pressure of $3 \cdot 10^{-7}$ mbar and a total exposure of 40 Langmuir (1 Langmuir is $10^{-6}$ Torr·s and 1 Torr is $1.332 \cdot 10^{-3}$ bar). Consecutively the sample is cooled down to room temperature forming the mesh as shown in figure 1.1.

## 1.3 Proposed Structure

The experimental group investigated the structure applying scanning tunneling microscopy (STM), low-energy electron diffraction (LEED) and ultraviolet photoelectron spectroscopy (UPS) [5]. According to the LEED pattern shown in figure 1.3 an in-plane lattice constant of 2.69 Å is found for the Rh(111) surface. A single layer of hexagonal boron nitride would have a lattice parameter of 2.48 ($\pm$ 0.05) Å, which already indicates that (due to the lattice mismatch) boron nitride does not grow epitaxially on top of the rhodium layer in contrast to nickel [2] on which it does. The LEED pattern shows additional spots indicating a super lattice with a periodicity of 32 ($\pm$ 1) Å, which corresponds to a 12×12 Rh unit cell that matches a 13×13 *h*-BN unit cell. According to the STM images (figure 1.1 and 1.2), which - as we know now - obviously suffered from some artefacts that could not be reproduced [6], a double layer model was proposed, according to which one layer forms an incomplete honeycomb structure on top of the rhodium surface followed by a second layer with additional holes leading to a partial double layer as shown in figure 1.4. This model explained in priniciple the image found in the STM experiments as well as the result of UPS (figure 1.5), which shows a splitting of the *h*-BN $\sigma$-bands (in contrast to the nickel case) into a $\sigma_1$ and a $\sigma_2$ contribution indicating two types of *h*-BN.

However, the proposed two layers model is unrealistic, since many broken

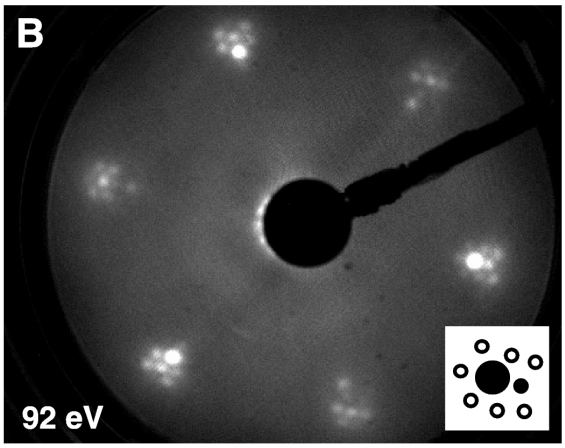


Figure 1.3: LEED pattern of the *h*-BN nanomesh on Rh(111) [5]

B-N bonds, which are energetically very unfavorable, would occur in the partial boron nitride layer. According to our DFT calculations [7] such broken bonds would only be stable if saturated e.g. with hydrogen atoms. Infrared spectroscopy (IR) could not detect any hydrogen atoms on the surface, but this does not exclude the presence of hydrogen because of the low sensitivity of this experiment. An additional problem with the two layer model is the corrugation derived from STM experiments, which is in the range from 0.5 to 1 Å (figure 1.2), a value much smaller than the interlayer distance of *h*-BN of 3.3 Å.

Such considerations led us to question the proposed two layer model. Consequently an alternative single layer model was introduced [7] which consists of only one - but highly corrugated - complete single layer (figure 1.6). The periodicity of the system contains a 12×12 Rh cell (as in the originally proposed double layer model), but on top of this layer a single *h*-BN layer is formed that consists of 13×13 *h*-BN unit cells. Due to the lattice mismatch between the rhodium surface and the *h*-BN layer the local topology (between

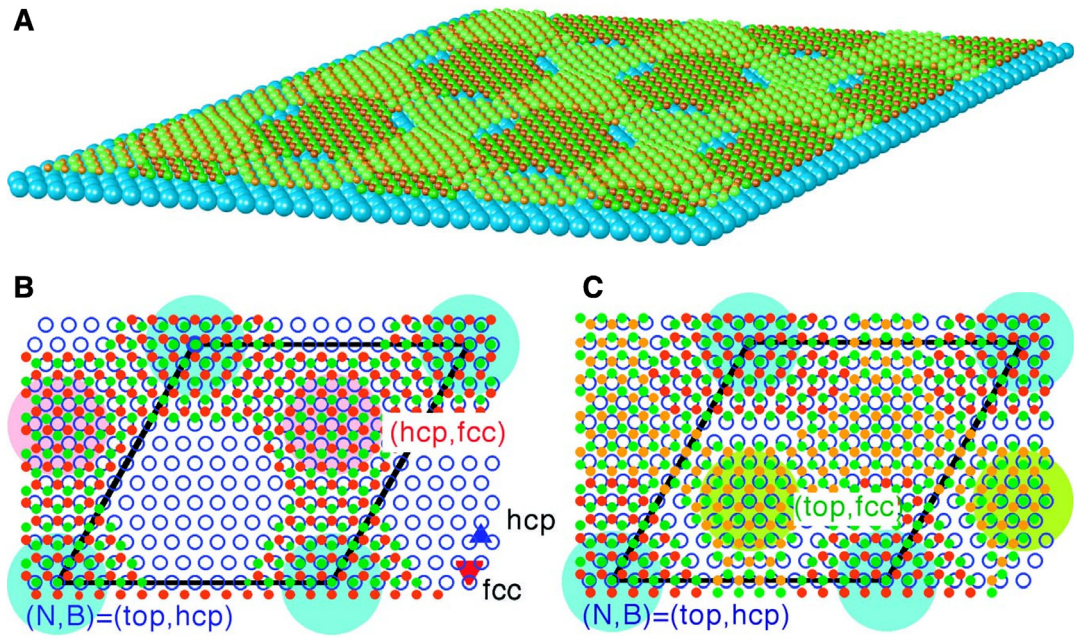


Figure 1.4: First proposed structure model of BN nanomesh on Rh(111) [5]. In the three dimensional image (A) the large blue balls represent the Rh(111) surface and the orange and green balls boron and nitrogen. The images show the two partial $h$-BN layers resulting in a corrugation of the surface, that still has areas of uncovered Rh(111). In the schematic top view (B) the first $h$-BN layer is illustrated, with the rhodium atoms as blue circles and boron and nitrogen as red and green dots. Additionally the geometric situation of boron and nitrogen with respect to the metal surface is indicated by the large colored circles. (See appendix A.2 for details.) In the third image (C) the second layer is shown additionally.

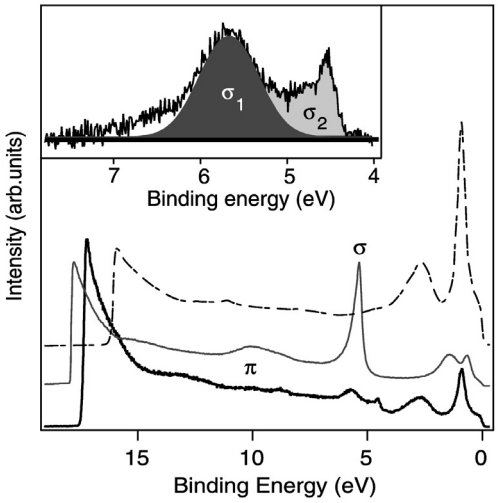


Figure 1.5: UPS spectum of the $h$-BN nanomesh on Rh(111) (thick solid line). For comparison also the spectra of the uncovered Ni(111) surface (dashed line) and $h$-BN/Ni(111) (thin solid line) are shown. The signals in the energy range from 0 to 4 eV come from the metal $d$ bands, at about 5 eV from the $h$-BN $\sigma$ bands and at approximately 10 eV from the $h$-BN $\pi$ states. Additionally the inset shows in detail the splitting of the $\sigma$ band of $h$-BN/Rh(111) in a $\sigma_1$ and a $\sigma_2$ contribution [5].

boron nitride and rhodium) changes continuously throughout the supercell resulting in different bonding situations between boron nitride and rhodium in the two layers, which causes a large corrugation of the system. This model is more favorable according to energetic considerations since neither broken bonds are present in *h*-BN nor hydrogen atoms are needed to saturate the dangling bonds. The geometry of this proposed single layer nanomesh model was first derived by an *ab initio* generated force field method [7]. The large size of this system made it necessary to make severe simplifications, so that this model may suffer from various approximations, which had to be done in order to reduce the computational effort. For example all force constants were derived from small unit cells, in which the *h*-BN layer was stressed to match the underlying Rh(111) surface. Another simplification was that the relaxation of the *h*-BN layer could only be evaluated with respect to the fixed rhodium surface. Therefore an influence of a relaxation of the rhodium interface could not be investigated.

The main goal of this thesis was to apply full DFT calculations to the proposed single layer model including relaxation of the top rhodium substrate layer.

Due to the large size of the system, conventional DFT calculations were not feasible at the beginning of this thesis and thus simpler schemes were necessary. After some search the software package OpenMX [8] was found, an order-N method, i.e the computational effort increases linearly with respect to the number of atoms. Other tested software packages were DFTB (Density Functional based Tight Binding) [9] and SIESTA (Spanish Initiative for Electronic Simulations with Thousands of Atoms) [10]. In order to carry out calculations with DFTB a proper set of parameter files has to be generated, which turned out to be problematic for the systems discussed in this work.

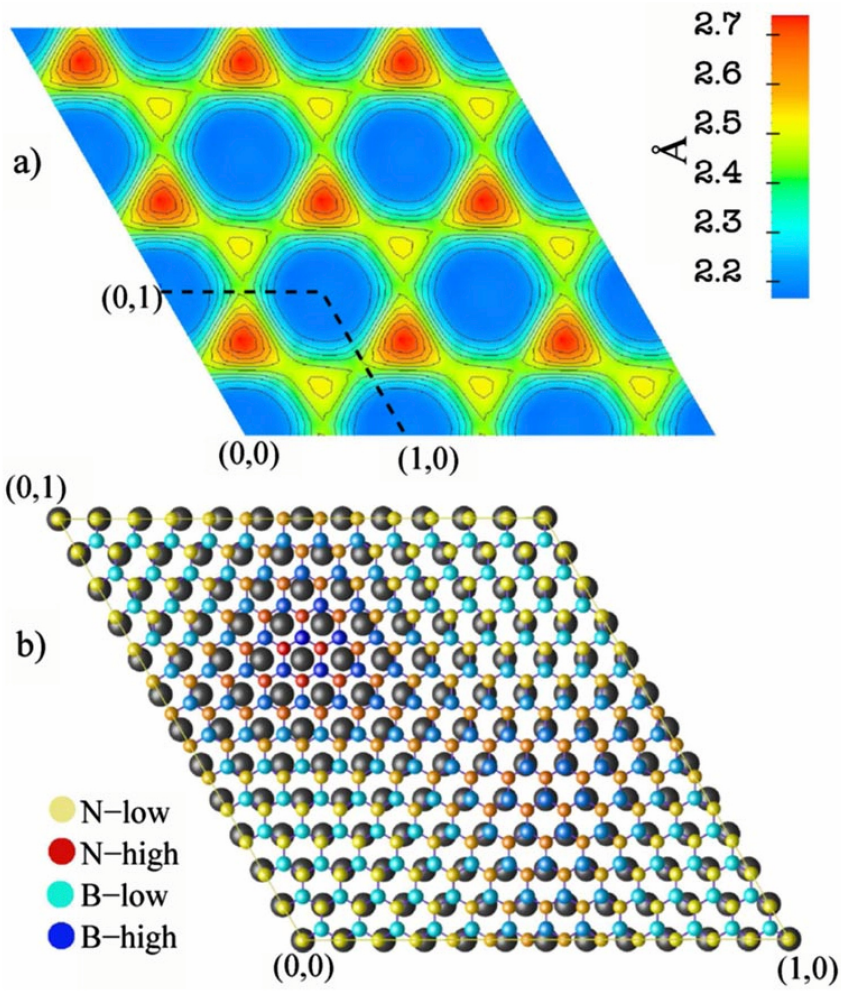


Figure 1.6: Newly proposed structure of the *h*-BN nanomesh on Rh(111) [7]. The first image (a) shows the corrugation of the system (with the rhombus indicating the unit cell). The second image shows the unit cell consisting of 12×12 Rh (gray balls) and 13×13 B-N cells. The boron atoms are colored in blue, with positons close to the metal in lightblue and positions with a large spacing in darkblue. The nitrogen atoms are colored from yellow for *low* positions to red for *high* positions.

The SIESTA program is also an order-N DFT code - like OpenMX - but is not capable of treating long range interactions as they occur in metals.

In comparison to the other software packages the main advantage of OpenMX is that it is capable to calculate large *metallic* systems within reasonable time, in contrast to conventional DFT calculations for which the effort increases with the third power of the system size (atoms or basis functions). At the end of this thesis it became possible to achieve a geometry relaxation also with WIEN2k [1, 11], due to a newly implemented iterative diagonalization scheme and greatly improved parallelization, which significantly reduced the computing time. These new results can now be compared with the still much faster (but less accurate) OpenMX calculations.

Although the simplified force field method mentioned above could be verified by the full DFT calculations for the *h*-BN nanomesh on Rh(111), preliminary results indicate that it failes for the nanomesh formed on Pt(111), which has an even larger lattice mismatch of 10.8 %. In the latter case the forces derived from a highly expanded *h*-BN (to match Pt(111)) are not transferable to unstrained *h*-BN. Therefore the platinum system has been investigated by both types of DFT calculations (OpenMX and WIEN2k) and the relaxation of the topmost interface layer was studied.

# Chapter 2

# Density Functional Theory

Within this chapter a short introduction of the applied methods and the fundamental physics will be given. The first part discusses the general basics of density functional theory (DFT). The second part gives a brief overview about the methods used in the two software packages WIEN2k and OpenMX used in this work. The fundamental concepts of the order-N scaling method will be described since OpenMX falls into this category.

## 2.1 General Introduction

### 2.1.1 The Schrödinger Equation

The Schrödinger equation is the fundamental equation of quantum mechanics as it describes the dependence of a quantum mechanical system in time and space. It is an axiom (just as the three Newton's laws) and was proposed in 1926 by Erwin Schrödinger (equation 2.1).

$$\left(\frac{-h^2}{8\pi^2 m}\nabla^2 + V\right)\Psi(\vec{r},t) = \frac{\hat{\imath}h}{2\pi}\frac{\partial\Psi(\vec{r},t)}{\partial t} \tag{2.1}$$

The drawback of this equation is that it can only be solved exactly for very simple systems, like the hydrogen atom. To be able to calculate more complex systems different approximations including numerical methods have to be introduced.

In general a solution for the ground state is desired which results in a time invariant problem. This leads to the *time independent* Schrödinger Equation (equation 2.2) which is the basis for most quantum mechanical *ab initio* calculations.

$$-\frac{\hbar}{2m}\nabla^2\psi(\vec{r}) + V(\vec{r})\psi(\vec{r}) = E\psi(\vec{r}) \tag{2.2}$$

A crucial point, which is difficult to handle, is the potential $V(\vec{r})$ which contains both, the classic Coulomb interaction between electrons and the nuclei and the electron electron interaction. The current state of the art method that handles these effects in an approximate but sufficiently accurate way is *Density Functional Theory* (DFT). As already indicated in the name this theory is based on the electron density of a system and not on its electronic wave functions $\psi(\vec{r})$, which is a complicated object depending on $3 \cdot n$ variables in a system with $n$ electrons. DFT is the method of choice for the calculations carried out in this thesis and thus a general overview about the approach and the implementation within large scale O(N) methods will be given in the next sections.

### 2.1.2 The Hohenberg-Kohn Theorems

According to the first Hohenberg and Kohn theorem [12] the ground state electron density $\rho(\vec{r})$ is a functional of an external potential $V_{\text{ext}}(\vec{r})$. Furthermore it can be shown that $V_{\text{ext}}(\vec{r})$ is - apart from a simple additive constant - uniquely defined by $\rho(\vec{r})$. This direct interrelation has the consequence that

an expectation value of an observable $A$ is also a unique functional of the electron density of the ground state.

$$< \Phi|\hat{A}|\Phi >= A[\rho] \tag{2.3}$$

This implies that all characteristics of a system that could be revealed from the electron wave functions can also be obtained from the electron density without any loss of information.

The second theorem states that the energy of an interacting inhomogeneous electron gas in the presence of an external potential $V_{\text{ext}}(\vec{r})$ is a functional of the electron density $\rho(\vec{r})$.

$$E_{V_{\text{ext}}}[\rho] = \int V_{\text{ext}}(\vec{r})\rho(\vec{r})d\vec{r} + F_{\text{HK}}[\rho] \tag{2.4}$$

The Hohenberg-Kohn density functional $F_{\text{HK}}[\rho]$ is a universal functional that is valid for any number of electrons and any external potential provided by the nuclei. It can be shown that the energy $E_{V_{\text{ext}}}[\rho]$ reaches its minimum for the ground state density corresponding to $V_{\text{ext}}(\vec{r})$, which implies that it is possible to use the variational principle of Rayleigh and Ritz to find the ground state energy. The variational principle states that the ground state energy $E_0$ is less or equal to the energy of the systems derived by a trial electron density $\tilde{\rho}$. Both energies would be equal if the trial electron density is identical to the density of the exact solution.

$$E_0 \leq E_V[\tilde{\rho}] \tag{2.5}$$

### 2.1.3 The Kohn-Sham equations

The Kohn-Sham equations [13] describe how a many-body system can be mapped to an one-electron reference system that leads to the same density

and thus energy as the real system,

$$E_{V_{\text{ext}}}[\rho] = T_0[\rho] + \int \rho(\vec{r}) V_{\text{ext}}(\vec{r}) d\vec{r} + \frac{1}{2} \iint \frac{\rho(\vec{r})\rho(\vec{r'})}{|\vec{r} - \vec{r'}|} d\vec{r} d\vec{r'} + E_{\text{xc}}[\rho] \quad (2.6)$$

where $T_0[\rho]$ is the functional for the kinetic energy of a non-interacting electron gas, the second term is the nucleus-electron Coulomb interaction, the third one is the Hartree contribution and the last $E_{\text{xc}}[\rho]$ is the exchange correlation energy. Resulting from the variational principle the Kohn-Sham theorem can now be expressed as an eigenvalue problem

$$\{-\frac{1}{2}\nabla^2 + V_{\text{ext}} + V_{\text{C}}(\rho(\vec{r})) + V_{\text{xc}}(\rho(\vec{r}))\}\Phi_i(\vec{r}) = \varepsilon_i \Phi_i(\vec{r}) \quad (2.7)$$

with an exchange correlation potential

$$V_{\text{xc}}(\rho(\vec{r})) = \frac{\partial E_{\text{xc}}(\rho(\vec{r}))}{\partial \rho(\vec{r})} \quad (2.8)$$

or in short

$$\hat{H}_{\text{KS}} \Phi_i = \varepsilon_i \Phi_i \quad (2.9)$$

where $\varepsilon_i$ are Lagrange multipliers resulting from the boundary condition of the orthogonality of the Kohn-Sham orbitals $\Phi_i$. It has to be mentioned that the single particle wave functions $\Phi_i$ do not describe real electron wave functions and have no strict physical meaning. Nevertheless the density resulting from the sum of these single electron wave functions is equal to the electron density of the real (interacting) system. As a further consequence the energies $\varepsilon_i$ are - strictly speaking - just Lagrange parameters but not equal to electron excitation energies, for which they are often used as a first approximation.

### 2.1.4 Exchange Correlation Energies and Potentials

While the equations 2.4 to 2.9 are still exact, $E_{\text{xc}}[\rho]$ is unknown. There are two main approaches to approximate this unknown exchange correlation

functional $E_{\mathrm{xc}}[\rho]$ mentioned above, which should include correction terms for the kinetic energy of independend particles and the corresponding self interaction from the Hartree term. The first is the so called *local density approach* (LDA)[14] (equation 2.10) which expresses the exchange correlation energy $E_{\mathrm{xc}}$ by an integration over the xc-energy density $\epsilon_{\mathrm{xc}}$ of a free homogeneous electron gas, which depends only on the local density $\rho(\vec{r})$.

$$E_{\mathrm{xc}}^{\mathrm{LDA}} = \int \rho(\vec{r})\epsilon_{\mathrm{xc}}\left(\rho(\vec{r})\right) d\vec{r} \tag{2.10}$$

The LDA potential (in equation 2.7) $V_{\mathrm{xc}}^{LDA} = \frac{\partial E_{\mathrm{xc}}}{\partial \rho}$ is widely used and gives good results in systems with a slowly varying electron density $\rho(\vec{r})$ but it is known to overestimate bonding in general.

The second commonly applied way to treat the exchange correlation energy is the *generalized gradient approximation* GGA which additionally takes the changes of the electron density $\rho(\vec{r})$ around a point $\vec{r}$ into account by including the gradient of the electron density $\nabla\rho(\vec{r})$.

$$E_{\mathrm{xc}}^{\mathrm{GGA}} = \int f(\rho(\vec{r}), \nabla\rho(\vec{r}))d\vec{r} \tag{2.11}$$

Due to the additional gradient term GGA often shows improvements over LDA but it tends to underestimate binding. Within this thesis the GGA exchange correlation potential by Perdew, Burke and Ernzerhof [15] is used exclusively. Therefore other DFT functionals are not discussed here.

## 2.2 Applied Methods

Within this work two different software packages were applied, which are both based on DFT but differ in the construction and type of wave functions leading to different advantages and drawbacks. The first software that is used

here is WIEN2k [16], which is a full potential DFT code that uses *augmented plane waves* as basis functions. It is a highly accurate program that allows to compute many different properties and carry out simulations of several spectroscopics. Especially for core level spectroscopies (where a core electron is excited into an unoccupied state) like the simulation of NEXAFS (Near Edge X-ray Absorption Fine Structure) it is necessary to include core states in the calculations and thus pseudopotential based methods cannot be applied (for details see chapter 3.1). The factor determining the computational effort is proportional to the third power of the number of atoms in the unit cell (or basis functions). Although this code is numerically highly efficient (with the recent improvements like fast iterative diagonalization schemes) the system size of the boron nitride nanomesh, containing at least about one thousand atoms is a real challenge for geometry optimization, requiring large computer time and memory.

Therefore in this thesis another software package OpenMX [8] was used which allows to optimize the geometry of such a large structure in reasonable time. The program belongs to the so called order-N methods, whose computational effort and the necessary memory scales linearly with the number of atoms in the unit cell. This package is based on pseudopotentials and uses a *linear combination of pseudo atomic orbitals* (LCPAO).

### 2.2.1 WIEN2k basis sets (LAPW and APW+lo)[1]

#### 2.2.1.1 Plane Waves (PW)

According to *Bloch's theorem* the eigenfunctions for a Hamiltonian with lattice periodicity can be written as the product of a function $u_{\vec{k}}^{n}(\vec{r})$ that has the periodicity of the lattice and a *phase factor* $\mathrm{e}^{i\vec{k}\cdot\vec{r}}$ with $\vec{k}$ being a vector

in the first Brillouin zone

$$\psi_{\vec{k}}^{n}(\vec{r}) = u_{\vec{k}}^{n}(\vec{r})\mathrm{e}^{\hat{\imath}\vec{k}\cdot\vec{r}} \tag{2.12}$$

where $n$ labels the band index. Within this equation the Bloch factor $\mathrm{e}^{\hat{\imath}\vec{k}\cdot\vec{r}}$ is known but the undetermined part $u_{\vec{k}}^{n}(\vec{r})$ has the periodicity of the lattice. Therefore the wave function $\psi_{\vec{k}}^{n}(\vec{r})$ can be written (according to a Fourier series) as the sum over *plane waves* of the same periodicity, which includes a sum of (all) reciprocal lattice vectors $\vec{K}$.

$$\psi_{\vec{k}}^{n}(\vec{r}) = \sum_{\vec{K}} c_{\vec{K}}^{n,\vec{k}}\mathrm{e}^{\hat{\imath}(\vec{k}+\vec{K})\cdot\vec{r}} \tag{2.13}$$

In order to find the wave function the coefficients $c_{\vec{K}}^{n,\vec{k}}$ must be determined. This basis set is complete and has the advantage of being unbiased and transferable but unfortunately it is very inefficient, since almost an infinite number of plane waves would be needed to properly describe the wavefunctions near the nucleus. Even for relative simple systems this would require a basis set of $10^8$ plane waves, leading to a matrix size of $10^8 \times 10^8$ that would have to be diagonalized. This is a size that cannot be handled at all with present computer systems.

#### 2.2.1.2 Linearized Augmented Plane Waves (LAPW)

The problem of the core like region in the wave function can be overcome by pseudopotentials and by an augmentation of the plane waves basis set. The idea behind the LAPW basis set is to avoid the introduction of pseudopotentials which simplify the calculations but looses information about the region near to the nucleus. The latter is of importance for example if one is interested in hyperfine fields or core level excitations. Since *plane waves* alone (chapter 2.2.1.1) would be by far too expensive, Slater suggested the

*augmented plane waves* (APW) method [17]. It partitions the unit cell into two types of regions: One part consists of atomic spheres $S_\alpha$ placed around each atom $\alpha$ and the other of the so called *interstitial region* $I$. These atomic spheres are also often called *muffin tin spheres*. Crystal wave functions are expanded into APW basis functions as

$$\psi^n_{\vec{k}}(\vec{r}, E) = \sum_{\vec{K}} c^{n,\vec{k}}_{\vec{K}} \cdot \phi^{\vec{k}}_{\vec{K}}(\vec{r}, E) \tag{2.14}$$

where $\phi^{\vec{k}}_{\vec{K}}(\vec{r}, E)$ are defined as

$$\phi^{\vec{k}}_{\vec{K}}(\vec{r}, E) = \begin{cases} \frac{1}{\sqrt{V}} \mathrm{e}^{\hat{\imath}(\vec{k}+\vec{K})\cdot\vec{r}} & \vec{r} \in I \\ \sum\limits_{\ell,m} A^{\alpha,\vec{k}+\vec{K}}_{\ell,m} u^\alpha_\ell(\mathsf{r}', E) Y_{\ell,m}(\vartheta(\vec{r}'), \varphi(\vec{r}')) & \vec{r} \in S_\alpha \end{cases} \tag{2.15}$$

$$\mathsf{r} := \|\vec{r}\| \tag{2.16}$$

with $\vec{K}$ beeing a vector of the reciprocal lattice and $V$ the volume of the unit cell. The position inside the sphere $\alpha$ is given by the vector $\vec{r}' = \vec{r} - \vec{r_\alpha}$ where $\vec{r_\alpha}$ is the position of the corresponding atom. The problem of this basis set lies in the energy dependence of $u^\alpha_\ell$ which are the solutions of the radial part of the Schrödinger equation in a given potential $V$ for an atom $\alpha$ at energy $E$. This makes the basis set energy depended. When $E$ equals the eigenvalue $\epsilon^n_{\vec{k}}$ of this state the (numerically) "exact" solution is found. However $E$ is not known when searching for eigenvalues. Mathematically this is a non-linear eigenvalue problem, which makes the APW method extremely demanding in computational terms.

To overcome this problem the energy dependence of the APW basis set has been linearized and thus the *linearized augmented plane wave*[18] method was introduced. The trick is to expand $u^\alpha_\ell(\mathsf{r}', E)$ into a sort of Taylor series around a fixed energy $E_\ell$, which is chosen near the center of the corresponding

band. This allows to approximate $u_\ell^\alpha(\mathsf{r}', E)$ when $E$ is near $E_\ell$.

$$u_\ell^\alpha(\mathsf{r}', E) = u_\ell^\alpha(\mathsf{r}', E_\ell) + (E - E_\ell) \underbrace{\frac{\partial u_\ell^\alpha(\mathsf{r}', E)}{\partial E}|_{E=E_\ell}}_{\dot{u}_\ell^\alpha(\mathsf{r}', E_\ell)} + \dots \tag{2.17}$$

Substituting $u_\ell^\alpha(\mathsf{r}', E)$ in the APW basis set with the first two terms of the Taylor series the resulting basis set has the form

$$\phi_{\vec{K}}^{\vec{k}}(\vec{r}) = \begin{cases} \frac{1}{\sqrt{V}} \mathrm{e}^{\hat{\imath}(\vec{k}+\vec{K})\cdot\vec{r}} & \vec{r} \in I \\ \sum\limits_{\ell,m} \left( A_{\ell,m}^{\alpha,\vec{k}+\vec{K}} u_\ell^\alpha(\mathsf{r}', E_\ell) + B_{\ell,m}^{\alpha,\vec{k}+\vec{K}} \dot{u}_\ell^\alpha(\mathsf{r}', E_\ell) \right) Y_{\ell,m}(\hat{r}) & \vec{r} \in S_\alpha \end{cases} \tag{2.18}$$

with the spherical harmonics

$$Y_{\ell,m}(\hat{r}) = Y_{\ell,m}(\vartheta(\vec{r}'), \varphi(\vec{r}')) \tag{2.19}$$

Now one has two parameters $A_{\ell,m}^{\alpha,\vec{k}+\vec{K}}$ and $B_{\ell,m}^{\alpha,\vec{k}+\vec{K}}$, that need to be determined by requiring that the atomic functions inside the spheres match the corresponding plane waves in value and slope at the sphere boundary. This *linearized augmented plane wave* (LAPW) scheme leads to a linear eigenvalue problem (that can be solved by a standard diagonalization). Unfortunately the LAPWs are less efficient than the APWs leading to a slower convergence of equation 2.14 than APW with the same number of $\vec{K}$ vectors. In practice the different $E_\ell$ values are chosen according to the center of gravity of each $\ell$ state (s,p,d,f) of each atom.

#### 2.2.1.3 Augmented Plane Waves and Local Orbitals (APW+lo)

As mentioned above the LAPW method needs more $\vec{K}$ vectors than the APW method and thus the latter would be favored but has the drawback of the energy dependence of the basis set. This led to a new formulation of the APW method [16] by adding *local orbitals* (lo) with two types of basis

functions which are combined for APW+lo. The first one are APWs but now with fixed energies $E_{1,\ell}^{\alpha}$

$$\phi_{\vec{K}}^{\vec{k}}(\vec{r}) = \begin{cases} \frac{1}{\sqrt{V}} \mathrm{e}^{\hat{\imath}(\vec{k}+\vec{K})\cdot\vec{r}} & \vec{r} \in I \\ \sum\limits_{\ell,m} A_{\ell,m}^{\alpha,\vec{k}+\vec{K}} u_{\ell}^{\alpha}(\mathsf{r}', E_{1,\ell}^{\alpha}) Y_{\ell,m}(\hat{r}) & \vec{r} \in S_{\alpha} \end{cases} \tag{2.20}$$

and the other ones are the *local orbitals* of the form

$$\phi_{\alpha,\mathrm{lo}}^{\ell,m}(\vec{r}) = \begin{cases} 0 & \vec{r} \notin S_{\alpha} \\ \left( A_{\ell,m}^{\alpha,\mathrm{lo}} u_{\ell}^{\alpha}(\mathsf{r}', E_{1,\ell}^{\alpha}) + B_{\ell,m}^{\alpha,\mathrm{lo}} \dot{u}_{\ell}^{\alpha}(\mathsf{r}', E_{1,\ell}^{\alpha}) \right) Y_{\ell,m}(\hat{r}) & \vec{r} \in S_{\alpha} \end{cases} \tag{2.21}$$

Note that within the APW and the lo basis the same set of energies $E_{1,\ell}^{\alpha}$ are used. The two coefficients $A_{\ell,m}^{\alpha,\mathrm{lo}}$ and $B_{\ell,m}^{\alpha,\mathrm{lo}}$ are determined by requiring that the local orbitals have zero value at the sphere boundary and are normalized to 1. This allows the determination of all eigenvalues with a basis set size of the APW method but using a simple diagonalization.

#### 2.2.1.4 Mixed LAPW/APW+lo Basis Set

Within the LAPW method it is more difficult to describe systems with valence d and f states (of atoms with relatively small muffin tin sphere) than with APW+lo using a certain number of plane waves. Therefore it is advantageous to use APW+lo only for those (difficult) states but use LAPW for all others. This combined basis set leads to accurate results but needs a significant smaller basis set (often half the size) which directly improves both the computational time and memory consumption. This mixed basis set was used in this thesis in all calculations carried out with WIEN2k.

### 2.2.2 OpenMX basis set and the (O)N Method

The software package OpenMX [8] is used within this thesis to run full DFT calculations with a linear scaling of the computational effort with respect to

the system size (number of atoms). This allowed the first DFT calculations of the *nanomesh* systems, which will be discussed later and is the main topic of this thesis. Therefore the following sections will give a short introduction about the principles to achieve linear scaling within DFT calculations.

#### 2.2.2.1 LCPAO Basis Set

The theoretical approach within the software package OpenMX is different to the method discussed before. In WIEN2k the basis set is mainly based on plane waves, which is the common method for many solid state calculations, whereas OpenMX uses the *linear combination of pseudoatomic orbitals* (LCPAO) [19]. The pseudo atomic orbitals $\phi_{i\alpha}$ are centered at the atomic sites $\vec{r}_i$ which lead to the Kohn-Sham Bloch functions $\psi^{\vec{k}}_{\sigma\mu}$

$$\psi^{\vec{k}}_{\sigma\mu}(\vec{r}) = \frac{1}{\sqrt{N}} \sum_{n}^{N} \mathrm{e}^{\hat{\imath}\cdot\vec{R}_n\cdot\vec{k}} \sum_{i\alpha} c^{\vec{k}}_{\sigma\mu,i\alpha} \phi_{i\alpha}(\vec{r} - \vec{r}_i - \vec{R}_n) \tag{2.22}$$

with $i$ the site index, $c$ the expansion coefficient, the spin index $\sigma$ and $\alpha \equiv (p, \ell, m)$ the orbital index. The values within the orbital index $\alpha$ determine the multiplicity index $p$ (number of eigenstates for same $\ell$ and $m$), the angular momentum quantum number $\ell$ and the magnetic quantum number $m$.

The corresponding pseudo atomic functions $\phi_{i\alpha}$ are a product of a real spherical harmonics $Y_{\ell m}$ and the numerical radial wave function $R_{p\ell}$

$$\phi_{i\alpha}(\vec{r}) = Y_{\ell m}(\vartheta(\vec{r}), \varphi(\vec{r})) \cdot R_{p\ell}(r) \tag{2.23}$$

which are eigenstates of an atomic Kohn-Sham equation. The pseudo atomic wave functions are determined by two parameters, the cutoff radius and the number of orbitals (eigenstates).

Additionally pseudopotentials are introduced which allow to replace the actual (real) deep core potentials with more shallow ones with the same slope

and value as the all electron potential at a defined distance from the atom center. This allows a much smaller basis set. The mandatory charge density $n^\sigma(\vec{r})$ associated with the spin component $\sigma$ is defined by the charge density operator $\hat{n}_\sigma$

$$\hat{n}_\sigma(\vec{r}) = \frac{1}{V_{\mathrm{BZ}}} \int\limits_{\mathrm{BZ}} dk^3 \sum_{\mu}^{\mathrm{occ}} |\psi^{\vec{k}}_{\sigma\mu}\rangle\langle\psi^{\vec{k}}_{\sigma\mu}| \tag{2.24}$$

with $\int\limits_{\mathrm{BZ}}$ the integration over the first Brillouin zone with volume $V_{\mathrm{BZ}}$ and $\sum\limits_{\mu}^{\mathrm{occ}}$ stands for the summation over all occupied states. By applying the operator the corresponding charge density $n_\sigma(\vec{r})$ is obtained

$$n^{(\sigma)}(\vec{r}) = \langle\vec{r}|\hat{n}_\sigma|\vec{r}\rangle \tag{2.25}$$

$$= \frac{1}{V_{\mathrm{BZ}}} \int\limits_{\mathrm{BZ}} dk^3 \sum_{\mu}^{\mathrm{occ}} \langle\vec{r}|\psi^{\vec{k}}_{\sigma\mu}\rangle\langle\psi^{\vec{k}}_{\sigma\mu}|\vec{r}\rangle \tag{2.26}$$

$$= \frac{1}{V_{\mathrm{BZ}}} \int\limits_{\mathrm{BZ}} dk^3 \sum_{n}^{N} \sum_{i\alpha,j\beta} \sum_{\mu}^{\mathrm{occ}} \mathrm{e}^{\hat{\imath}\cdot\vec{R}_n\cdot\vec{k}} c^{\vec{k}\,\star}_{\sigma\mu,i\alpha} c^{\vec{k}}_{\sigma\mu,j\beta} \phi_{j,\beta}(\vec{r}-\vec{r}_j)\phi_{i,\alpha}(\vec{r}-\vec{r}_i-\vec{R}_n) \tag{2.27}$$

$$= \sum_{n}^{N} \sum_{i\alpha,j\beta} \rho^{\vec{R}_n}_{\sigma,i\alpha,j\beta} \phi_{i,\alpha}(\vec{r}-\vec{r}_i)\phi_{j,\beta}(\vec{r}-\vec{r}_j-\vec{R}_n) \tag{2.28}$$

with the density matrix defined as

$$\rho^{\vec{R}_n}_{\sigma,i\alpha,j\beta} = \frac{1}{V_{\mathrm{BZ}}} \int\limits_{\mathrm{BZ}} dk^3 \sum_{\mu}^{\mathrm{occ}} \mathrm{e}^{\hat{\imath}\cdot\vec{R}_n\cdot\vec{k}} c^{\vec{k}\,\star}_{\sigma\mu,i\alpha} c^{\vec{k}}_{\sigma\mu,j\beta} \tag{2.29}$$

Furthermore a difference charge density $\delta n_\sigma(\vec{r})$ is introduced

$$\delta n_\sigma(\vec{r}) = n_\sigma(\vec{r}) - n^{(a)}_\sigma(\vec{r}) \tag{2.30}$$

$$\delta n_\sigma(\vec{r}) = n_\sigma(\vec{r}) - \sum_i n^{(a)}_{i,\sigma}(\vec{r}) \tag{2.31}$$

with $n^{(a)}_\sigma(\vec{r})$ the atomic charge density derived from an *isolated* atom associated with site $i$. This is important for the linear scaling algorithm as will

be discussed in the next section. It has to be noted that the overall atomic charge density $n_\sigma^{(a)}(\vec{r})$ is just the sum of its atomic contributions $n_{i,\sigma}^{(a)}(\vec{r})$ resulting from the pseudo atomic orbitals $\phi$ and the atomic density matrix $\rho$ defined in equation 2.44:

$$n_\sigma^{(a)}(\vec{r}) = \sum_{i\alpha,j\beta} \phi_{i\alpha}(\vec{r})\phi_{j\beta}(\vec{r})\rho_{i\alpha,j\beta}^{(\sigma)} \tag{2.32}$$

$$= \sum_i n_{i,\sigma}^{(a)}(\vec{r}) \tag{2.33}$$

The total energy $E_{\text{tot}}$ determined for the calculated system is the sum of the kinetic energy $E_{\text{kin}}$, the electron-core Coulomb energy $E_{\text{ec}}$, the electron-electron Coulomb energy $E_{\text{ee}}$, the exchange correlation energy $E_{\text{xc}}$ and the core-core Coulomb energy $E_{\text{cc}}$

$$E_{\text{tot}} = E_{\text{kin}} + E_{\text{ec}} + E_{\text{ee}} + E_{\text{xc}} + E_{\text{cc}} \tag{2.34}$$

with the kinetic energy given by the kinetic energy operator $\hat{T}$

$$E_{\text{kin}} = \frac{1}{V_{\text{BZ}}} \int_{\text{BZ}} dk^3 \sum_\sigma \sum_\mu^{\text{occ}} \langle \psi_{\sigma\mu}^{\vec{k}} | \hat{T} | \psi_{\sigma\mu}^{\vec{k}} \rangle \tag{2.35}$$

Due to the use of pseudopotentials the electron-core Coulomb energy $E_{\text{ec}}$ consists of two different contributions $E_{\text{ec}}^{(L)}$ and $E_{\text{ec}}^{(NL)}$, which are either related to the local or to the non-local parts of the pseudopotentials (for details see [20]). The electron-electron Coulomb energy $E_{\text{ee}}$ is obtained by

$$E_{\text{ee}} = \frac{1}{2} \iint dr^3 dr'^3 \frac{n(\vec{r})n(\vec{r'})}{|\vec{r} - \vec{r'}|} \tag{2.36}$$

$$= \frac{1}{2} \int dr^3 n(\vec{r}) V_{\text{H}}(\vec{r}) \tag{2.37}$$

$$= \frac{1}{2} \int dr^3 n(\vec{r}) \left( V_{\text{H}}^{(a)}(\vec{r}) + \delta V_{\text{H}}(\vec{r}) \right) \tag{2.38}$$

with $V_{\text{H}}$ split into two parts $V_{\text{H}}^{(a)}$ and $\delta V_{\text{H}}$, which are a result of the atomic charge densities $n^{(a)}(\vec{r})$ and the difference charge density $\delta n(\vec{r})$ (the index $\sigma$

for the spin is omitted, since the total electron contribution is considered) defined by

$$V_{\mathrm{H}}^{(a)} = \sum_i \int dr'^3 \frac{n_i^{(a)}(\vec{r})}{\vec{r} - \vec{r'}} \tag{2.39}$$

$$= \sum_i V_{\mathrm{H},i}^{(a)}(\vec{r} - \vec{r}_i) \tag{2.40}$$

$$\delta V_{\mathrm{H}}(\vec{r}) = \int dr'^3 \frac{\delta n(\vec{r})}{\vec{r} - \vec{r'}} \tag{2.41}$$

The exchange correlation energy $E_{\mathrm{xc}}$ is defined by the GGA functional [15] and the core-core Coulomb energy $E_{\mathrm{cc}}$ is derived by the repulsive Coulomb forces resulting from the effective core charges $Z_i$ determined in the generated pseudopotential by

$$E_{\mathrm{cc}} = \frac{1}{2} \sum_{i,j} \frac{Z_i Z_j}{\vec{r}_i - \vec{r}_j} \tag{2.42}$$

While most of the energy contributions can be reduced to two center integrals by applying a projector expansion [21], the long range contribution of the electron-electron Coulomb energy and the exchange-correlation energy are evaluated on a real regular mesh. The fineness (i.e. the number of grid points) of this mesh is determined by a plane waves cutoff energy $E_{cut}$.

To be able to relax the geometric structure the atomic forces have to be evaluated. The forces on an atom $i$ with respect to its position $\vec{r}_i$ are calculated by

$$\vec{F}_i = -\frac{\partial E_{\mathrm{tot}}}{\partial \vec{r}_i} \tag{2.43}$$

where $\frac{\partial E_{\mathrm{tot}}}{\partial \vec{r}_i}$ can be determined by calculating the partial derivatives of the energies contributing to the total energy $E_{\mathrm{tot}}$ [20].

#### 2.2.2.2 Linear Scaling Algorithm

In order to solve large systems a new approach is introduced in which the computational effort scales linearly with system size; in short O(N). In con-

ventional DFT calculations the charge density is derived from the quasi particle wave functions. But in contrast the implemented O(N) algorithm in OpenMX reveals the density matrix with the help of Green's functions. The so called O(N) Krylov-subspace method [22] applied in this software package is a combination of the *divide-and-conquer* (DC) method [23, 24, 25] and the *recursion method* [26, 27, 28, 29, 30] based on the Lanczos algorithm [31]. The benefit of the DC method is that it provides a rapid convergence but only for covalent systems like biological molecules. The reason for this limitation is that the local density matrix cannot handle the long range interaction as it occurs in metallic systems [32]. In contrast to that scheme the recursion method is an appropriate method for calculating metals, but it is unstable when applied to an SCF iteration. The Krylov-subspace method described in this chapter combines the advantages of both approaches and thus allows fast SCF calculation of large metallic systems.

The concept of Green's functions results from the approach to describe quantum mechanical systems not in terms of wave functions, like it is done when using Schrödingers equation, but using scattering theory [33]. The density matrix can be expressed in terms of Green's functions $\mathcal{G}^{(\sigma)}_{i\alpha,j\beta}$ by

$$\rho^{(\sigma)}_{i\alpha,j\beta} = -\frac{1}{\pi}\mathrm{Im}\int \mathcal{G}^{(\sigma)}_{i\alpha,j\beta}(E+\hat{\imath}\xi)\, f\left(\frac{E-\mu}{k_B T}\right) dE \tag{2.44}$$

with the Fermi function $f(x)$,

$$f(x) := \frac{1}{1+\exp(x)} \tag{2.45}$$

an infinitesimal small positive $\xi$

$$\xi := \lim_{k\to\infty}\frac{1}{k} \qquad k \in \mathbb{R} \tag{2.46}$$

and the chemical potential $\mu$. The advantage of this type of functions is that the common function, which is necessary for evaluating the overall density

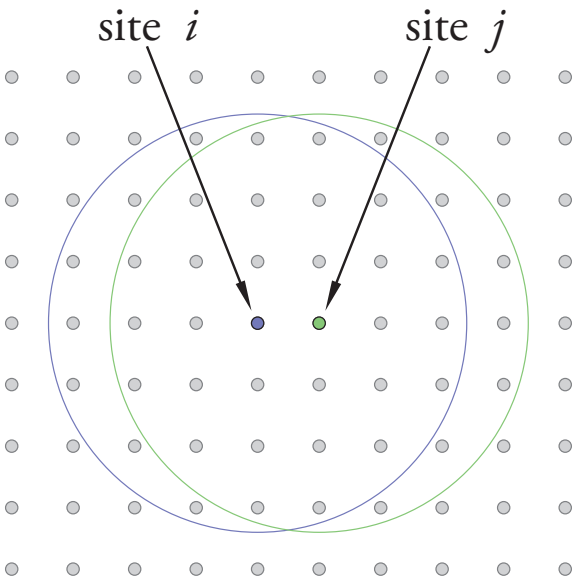


Figure 2.1: Schematic view of truncated clusters [22]

of a system, can easily be constructed as the sum of parts of functions. This possibility of using a *patchwork* of Green's functions allows to split a large system in smaller parts that are combined afterwards as applied in the DC algorithm [23, 24, 34], with the assumption that the total density of states can be approximated by the sum of local density of states of the central atom in each site. This is the mandatory step which makes linear scaling possible.

In more detail the whole (large) system is truncated into clusters around each site as shown in figure 2.1 [22], where the clusters are allowed to largely overlap. Fur a further improvement OpenMX does not apply the common method of the *physical truncation* where all atoms within a defined range around the central site are taken into account but selects the atoms in a more sophisticated way. They are determined using the *logical truncation* scheme by considering the distance of atoms which are regarded of forming a

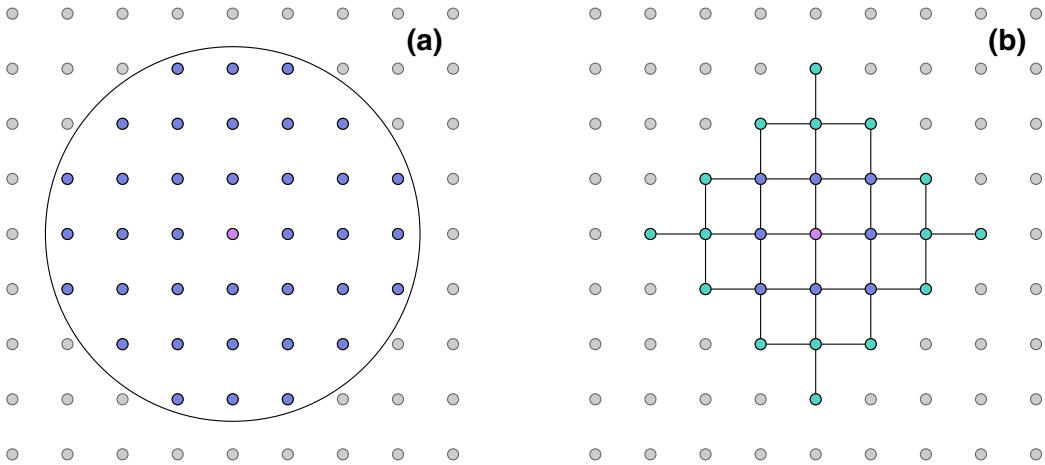


Figure 2.2: Comparison between the (a) physically and (b) logically truncated clusters of a regular square lattice. For the physical truncation all atoms within a sphere of a given radius are selected. The logical truncation scheme selects all atoms in a shorter - bond like - range and proceeds from these atoms in the same way until a defined depth is reached.

bond. To select the atoms within the cluster all atoms within a certain bond range (*hopping range*) around the central site are included and afterwards one proceeds in the same way until a defined depth is reached (*number of hoppings*). A schematic view comparing the two different methods is shown in figure 2.2. For each of this generated smaller systems (with the central site $i$) both the local Hamiltonian $\hat{H}^{(i)}$ and the local overlap matrix $S^{(i)}$ are constructed.

By diagonalization of the local eigenvalue problem

$$\hat{H}^{(i)} c_\mu^{(i)} = \varepsilon_\mu^{(i)} S^{(i)} c_\mu^{(i)} \tag{2.47}$$

the resulting eigenvalues and eigenstates allow the simple construction of the

local Green's function as described in equation 2.48 (due to easier notation the index ($\sigma$) is omitted)

$$\mathcal{G}_{i\alpha,j\beta}(Z) = \sum_{\mu} \frac{c_{\mu,i\alpha} c^*_{\mu,j\beta}}{Z - \varepsilon_\mu} \tag{2.48}$$

with the complex number $Z$ resulting in poles of $\mathcal{G}_{i\alpha,j\beta}(Z)$ if equal to the eigenvalues $\varepsilon_\mu$.

In order to achieve a further reduction in computational effort not a direct diagonalization is carried out but an iterative diagonalization scheme is applied as it is done in the approach of the recursion method. By performing a two-sided Lanczos algorithm the matrix is mapped to a Krylov subspace $\mathbf{U}_\mathrm{K}$

$$\mathbf{U}_\mathrm{K} = \mathrm{span}\left\{|e\rangle, A|e\rangle, A^2|e\rangle, \ldots, A^q|e\rangle\right\} \tag{2.49}$$

with $A := (S^{(i)})^{-1}\hat{H}^{(i)}$, $q$ the recursion depth of the Lanczos transformation and $|e\rangle = (|e_1\rangle, |e_2\rangle, \ldots, |e_{M_i}\rangle)$ with the basis orbitals $|i\alpha\rangle$ at site $i$ having $M_i$ basis functions. This is a significant improvement since the dimension of the resulting matrix, which is necessary to achieve sufficient accuracy, is in general much smaller than that of the full matrix of the truncated cluster. This has a large effect to the computational effort, since the diagonalization still scales with the third power of the matrix size.

Furthermore the truncated cluster is divided into a core and a buffer region. The core region is defined by those sites which have an overlap of $\chi_{i\alpha}\chi_{j\beta}$ that is non zero with the center site $i$. Due to a orthogonal transformation, which assures that $\mathbf{U}^\dagger_\mathrm{K} S \mathbf{U}_\mathrm{K} = I$ [22], the generalized eigenvalue problem

$$\hat{H} c_\mu = \varepsilon_\mu S c_\mu \tag{2.50}$$

can be transformed to a standard eigenvalue problem

$$\hat{H}^\mathrm{K} b_\mu = \varepsilon_\mu b_\mu \tag{2.51}$$

with

$$\hat{H}^{\mathrm{K}} = \mathbf{U}_{\mathrm{K}}^{\dagger}\hat{H}\mathbf{U}_{\mathrm{K}} \tag{2.52}$$

$$= u_c^{\dagger}\hat{H}_c u_c + u_c^{\dagger}\hat{H}_{cb}u_b + u_b^{\dagger}\hat{H}_{cb}^{\dagger}u_c + u_c^{\dagger}\hat{H}_b u_b \tag{2.53}$$

$$= \hat{H}_{\mathrm{s}}^{\mathrm{K}} + \hat{H}_{\mathrm{l}}^{\mathrm{K}} \tag{2.54}$$

with $H_c$, $H_b$ and $H_{cb}$ the Hamiltonian matrices for the core region, the buffer region and the region between core and buffer. Thus the Krylov subspace is split into a core and a buffer region $\mathbf{U}_{\mathrm{K}}^{\dagger} = (u_c^{\dagger}; u_b^{\dagger})$ and therefore also the Hamiltonian $\hat{H}^{\mathrm{K}}$ is decomposed in two parts consisting of a short range $\hat{H}_s^{\mathrm{K}}$ and a long range $\hat{H}_l^{\mathrm{K}}$ contribution.

To achieve sufficient accuracy - especially for metallic systems - the long range contribution $\hat{H}_l^{\mathrm{K}}$ is calculated at the first SCF step and kept fixed during the further iteration and updated after self consistency. For the other SCF steps the standard eigenvalue problem is diagonalized with an updated $\hat{H}_s^{\mathrm{K}}$ and the fixed $\hat{H}_l^{\mathrm{K}}$. Thus a detailed short range contribution is derived by taking an effective correction by the long range contribution into account.

According to equation 2.33 the elements with non zero overlap at site $i$ contribute to the charge density and the corresponding matrix elements can easily be obtained by the back transformation

$$c_\mu = u_c b_\mu \tag{2.55}$$

In the next step a common chemical potential for all truncated clusters of the system is found. This is done by representing the Green's functions in terms of Mulliken populations

$$\mathcal{G}_i(Z) = \sum_{\alpha,j\beta} \mathcal{G}_{i\alpha,j\beta}(Z) S_{j\beta,i\alpha} = \sum_{\mu} \frac{\kappa_\nu^{(i)}}{Z - \varepsilon_\mu^{(i)}} \tag{2.56}$$

with

$$\kappa_\nu^{(i)} = \sum_{\alpha,j\beta} c_{\mu,i\alpha} c_{\mu,j\beta}^{*} S_{j\beta,i\alpha} \tag{2.57}$$

allowing an exchange of electrons between the truncated clusters. In the last step the charge density of the whole system is determined by equation 2.33 and the Hartree potential is evaluated by solving Poisson's equation using a fast Fourier transformation.

#### 2.2.2.3 Implementation

This section describes how the previously discussed models are implemented in the software package and how calculations are carried out [22]. It has to be mentioned that only in the first SCF cycle the logical truncation of the system is determined (step 1) and the Krylov subspace (step 3) is generated. They are kept fixed until self consistency.

1. Logical Truncation of the System

   The large system is split up into smaller subsystems using the logical truncation scheme by a defined number and range of hoppings. (See the previous section for details.)

2. Construction of the local Hamiltonian

   For each of the smaller sub systems the local Hamiltonian and overlap matrix is generated. This is done as in conventional DFT calculations but additionally the Hartree potential of the large system is included in the local configuration. Therefore an isolation of the sub system and thus the neglect of long range Coulomb contributions is omitted.

3. Generation of the Krylov Subspace

   The Krylov Subspace $\mathbf{U}_\mathrm{K}$ is generated once using the two sided Lanczos algorithm and is stored until selfconsistency is reached. This step is necessary in order to avoid the numerical fluctuations during the SCF

cycle, which would occur applying only the recursion method to an iterative scheme.

4. Construction of the effective Hamiltonian

   The effective Hamiltonian of each subsystem is constructed taking the long range contributions (of the whole system) into account.

5. Check for Selfconsistency

   The eigenvalue problem with the effective Hamiltonian is diagonalized resulting in a set of components of eigenvectors, which allows to calculate the necessary overall charge density and the common chemical potential.

### 2.2.3 Geometry Optimization with OpenMX

In this section the different algorithms for geometry optimization will be discussed, which were used in this work to relax the geometric structure with the software package OpenMX [35].

#### 2.2.3.1 Newton Method

In order to find the optimum geometry of a system, the total energy $E_{\mathrm{tot}}$ is expanded into a Taylor series with respect to the atomic positions $\vec{r}_i$ near the calculated energy $E_0$, which is related to the coordinates $\vec{r}_{i_0}$. The resulting equation is

$$\begin{aligned} E = E_0 \quad & + \sum_{i}^{3N} \left( \frac{\partial E}{\partial \vec{r}_i} \right)_0 (\vec{r}_i - \vec{r}_{i_0}) + \\ & + \frac{1}{2} \sum_{i,j}^{3N} \left( \frac{\partial^2 E}{\partial \vec{r}_i \partial \vec{r}_j} \right)_0 (\vec{r}_i - \vec{r}_{i_0})(\vec{r}_j - \vec{r}_{j_0}) + \ \ldots \end{aligned} \tag{2.58}$$

with N the number of atoms and $()_0$ indicating the partial derivatives at the coordinates $\vec{r}_{i_0}$. Differentiating equation 2.58 with respect to the atomic

positions $\vec{r}_k$ and - taking into account only the terms up to the second order - gives

$$\frac{\partial E}{\partial \vec{r}_k} = \left(\frac{\partial E}{\partial \vec{r}_k}\right)_0 + \sum_i^{3N} \left(\frac{\partial^2 E}{\partial \vec{r}_k \partial \vec{r}_i}\right)_0 (\vec{r}_i - \vec{r}_{i_0}) \tag{2.59}$$

with the derivative $\frac{\partial E}{\partial \vec{r}_k}$ determining the force on the atom (equation 2.43). If the atomic positions $\vec{r}_k$ are in a local minimum, the resulting force is 0 and thus the derivative $\frac{\partial E}{\partial \vec{r}_k}$ becomes 0. According to this the following equation can be set up:

$$\begin{pmatrix} \left(\frac{\partial^2 E}{\partial \vec{r}_1 \partial \vec{r}_1}\right)_0 & \left(\frac{\partial^2 E}{\partial \vec{r}_1 \partial \vec{r}_2}\right)_0 & \cdots \\ \left(\frac{\partial^2 E}{\partial \vec{r}_2 \partial \vec{r}_1}\right)_0 & \left(\frac{\partial^2 E}{\partial \vec{r}_2 \partial \vec{r}_2}\right)_0 & \cdots \\ \cdots & \cdots & \cdots \end{pmatrix} \begin{pmatrix} (\vec{r}_1 - \vec{r}_{1_0}) \\ (\vec{r}_2 - \vec{r}_{2_0}) \\ \cdots \end{pmatrix} = - \begin{pmatrix} \left(\frac{\partial E}{\partial \vec{r}_1}\right) \\ \left(\frac{\partial E}{\partial \vec{r}_2}\right) \\ \cdots \end{pmatrix} \tag{2.60}$$

which can be written in short form as

$$\mathbf{H}\Delta\vec{r} = -\vec{g} \tag{2.61}$$

with $\mathbf{H}$ the Hessian matrix consisting of the second derivatives. The differences in atomic positions $\Delta\vec{r}$ between two geometry optimization steps can be expressed as

$$\Delta\vec{r} = \vec{r}_{(n+1)} - \vec{r}_{(n)} \tag{2.62}$$

and thus the next geometric position can be determined by

$$\vec{r}_{(n+1)} = \vec{r}_{(n)} - \mathbf{H}^{-1}_{(n)}\vec{g}_{(n)} \tag{2.63}$$

The Newton method is a very robust scheme but has the disadvantage that convergence is rather slow, resulting in a large number of geometry optimization steps, which are necessary to achieve a sufficient relaxation.

#### 2.2.3.2 RMM-DIIS

To achieve an improvement with respect to the necessary geometry optimization steps the Newton algorithm discussed above is expanded. The *residual*

*minimization method in the direct inversion of iterative subspace* (RMM-DIIS) [36, 37] introduces a tuning parameter $\alpha$ to equation 2.63 and gives

$$\vec{r}_{(n+1)} = \vec{r}_{(n)} - \alpha\, \mathbf{H}^{-1}_{(n)} \vec{g}_{(n)} \tag{2.64}$$

which allows to accelerate convergence. Within the RMM-DIIS algorithm $\vec{g}_{(n)}$ is determined by a linear combination of the $p$ previous gradients derived by the Newton method $\vec{g}_{N(n)}$

$$\vec{g}_{(n)} = \sum_{m=n-(p-1)}^{n} a_m \vec{g}_{N(m)} \tag{2.65}$$

The factors $a_m$ are determined by minimizing $\langle \vec{g}_{(n)} | \vec{g}_{(n)} \rangle$ and constraining

$$\sum_{m=n-(p-1)}^{n} a_m = 1 \tag{2.66}$$

Computationally this is done by the *Lagrange's multipliers method* solving the function $F$ defined by

$$F = \langle \vec{g}_{(n)} | \vec{g}_{(n)} \rangle - \lambda \left( 1 - \sum_{m=n-(p-1)}^{n} a_m \right) \tag{2.67}$$

With the derived coefficients $a_m$ an optimum choice for $\vec{r}_{(n)}$ is obtained:

$$\vec{r}_{(n)} = \sum_{m=n-(p-1)}^{n} a_m \vec{r}_{(m)} \tag{2.68}$$

The Hessian matrix $\mathbf{H}$ in equation 2.64 is approximated by the unit matrix $\mathbf{I}$ and thus the next atomic positions can be derived by

$$\vec{r}_{(n+1)} = \vec{r}_{(n)} - \alpha\, \vec{g}_{(n)} \tag{2.69}$$

This method showed to be an advantage for optimizing the geometry of molecules like borazin, which was calculated in this work applying the RMM-DIIS scheme. But for large structures like the nanomesh formed on Rh(111) and Pt(111) it tends to over-correct the next atomic positions which resulted in the occasional destruction of the structure.

#### 2.2.3.3 Eigenvector Following Method

The Eigenvector following method is based on the RMM-DIIS scheme but in this case the Hessian $\mathbf{H}$ in equation 2.64 is not roughly approximated by the unit matrix $\mathbf{I}$ but by the method of Broyden-Fletcher-Goldfarb-Shanno (BFGS) [38, 39, 40, 41] and the rational function (RF) algorithm [42]

$$\mathbf{H}_{(n)} = \mathbf{H}_{(n-1)} + \frac{|\Delta\vec{g}_{(n)}\rangle\langle\Delta\vec{g}_{(n)}|}{\langle\Delta\vec{r}_{(n)}|\Delta\vec{g}_{(n)}\rangle} - \frac{\mathbf{H}_{(n-1)}|\Delta\vec{r}_{(n)}\rangle\langle\Delta\vec{r}_{(n)}|\mathbf{H}_{(n-1)}}{\langle\Delta\vec{r}_{(n)}|\mathbf{H}_{(n-1)}|\Delta\vec{r}_{(n)}\rangle} \tag{2.70}$$

with

$$\Delta\vec{g}_{(n)} = \vec{g}_{(n)} - \vec{g}_{(n-1)} \tag{2.71}$$

$$\Delta\vec{r}_{(n)} = \vec{r}_{(n)} - \vec{r}_{(n-1)} \tag{2.72}$$

which suffers from the ill-conditioned approximated inverse of the Hessian matrix $\mathbf{H}_{(n)}$ having negative eigenvalues. To overcome this problem first the actual eigenvalues of the resulting Hessian are calculated

$$\mathbf{E}_{(n)} = \mathbf{V}_{(n)}^{\mathrm{T}}\mathbf{H}_{(n)}\mathbf{V}_{(n)} \tag{2.73}$$

with $\mathbf{E}_{(n)}$ being the diagonal matrix with the eigenvalues of $\mathbf{H}_{(n)}$ and the potential $\mathbf{V}_{(n)}$. To improve the Hessian $\mathbf{H}_{(n)}$ all eigenvalues below a specific threshold (for OpenMX calculations 0.02 a.u.) are set to the thresholds value. With this modified eigenvalue matrix $\mathbf{E}'_{(n)}$ a corrected Hessian is calculated

$$\mathbf{H}'^{-1}_{(n)} = \mathbf{V}_{(n)}\mathbf{E}'^{-1}_{(n)}\mathbf{V}_{(n)}^{\mathrm{T}} \tag{2.74}$$

which will be used for updating the atomic position in equation 2.64. This scheme showed to be a robust but still rather fast method and thus was mainly used in this work.

# Chapter 3

# Simulation of NEXAFS Spectra

## 3.1 NEXAFS Spectroscopy

NEXAFS (Near Edge X-ray Absorption Fine Structure) is an electron spectroscopy, that is element specific and allows to probe the amount, orientation and chemical bonding of various atoms in molecules, surfaces and bulk materials.

The underlying principle of NEXAFS spectroscopy is the excitation of a core electron into an unoccupied state according to dipol selection rules. A schematic drawing of this method is shown in figure 3.1. A photon of X-ray energy ($h \cdot \nu$) is absorbed and excites a core electron ($e^-$) with angular momentum $\ell$ into an unoccupied state with $\ell \pm 1$ - between the Fermi level ($E_\mathrm{F}$) and the ionization potential ($E_\mathrm{IP}$). The part of the spectrum containing this specific form of transition is located near of the absorption edge with a range of about 50 eV. The resulting core hole is filled quickly by relaxation of an electron from a higher level by emission of either a fluorescent photon or an Auger electron. The absorption edge is characteristic for a specific element and the shell from which the electron is excited. Within this thesis

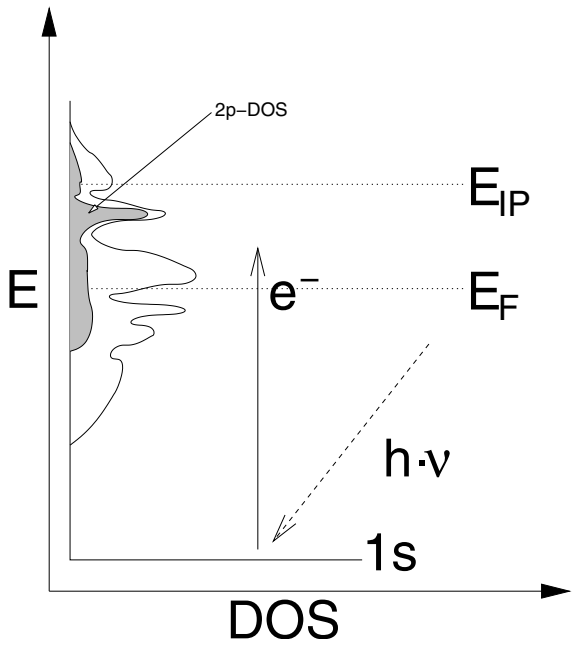


Figure 3.1: Schematic drawing of the excitation in NEXAFS spectroscopy

only spectra resulting from the excitation of an 1$s$ core electron into empty 2$p$ states will be discussed, especially for the atoms boron and nitrogen. The resulting notation of the absorption edges are therefore B-K and N-K.

## 3.2 Theoretical Method

For the derivation of B-K and N-K NEXAFS spectra the *final state rule* [43] is used. It states that the electronic states after the transition into the unbound states determine the spectrum, i.e. when the states are allowed to feel the influcence of the core hole. Therefore a self consistend DFT calculation is performed for a system (often within a bigger supercell), in which an atom with a core hole is present, because the core electron has been excited into the conduction band. The use of supercells is necessary

since in reality only a very low fraction of atoms is excited simultaneously during such experiments. According to Slater's *transition state rule* [44, 45] the best results are expected for calculations with half a core hole, since the excitation energy for an electron is approximately equal to the eigenvalue of the relaxed state of its half occupied orbital (equation 3.1).

$$\Delta E_\alpha|_{\mathrm{rel}} \approx \varepsilon_\alpha(\frac{1}{2}) \tag{3.1}$$

Based on such an electron configuration and the corresponding densities of states the intensity of the theoretical absorption spectrum [46] is calculated according to Fermi's golden rule using equation 3.2.

$$I \propto \nu^3 \left| \left\langle \Psi^{\mathrm{val}}_{A,l\pm1} \left| r \right| \Psi^{\mathrm{core}}_{A,n,l} \right\rangle \right|^2 \chi^A_{l\pm1}(\varepsilon)\ \delta(\varepsilon - E_{\mathrm{core}}, h\nu) \tag{3.2}$$

It shows that the absorption is proportional to the third power of the photon frequency $\nu$, the square of the dipole matrix element involving the dipole operator $r$, the core and the conducting band wave functions and the proper partial density of states $\chi$ of the corresponding atom A. The last term expresses the energy conservation. Furthermore the dipole selection rules allow only transitions between states with a difference in the azimuthal quantum number $\Delta\ell$ of $\pm1$. Due to the involvement of the core sates in the dipole matrix element the absorption becomes site specific, which allows to probe specifically the electronic structure of the excited atom.

# Part IV

# Results and Discussion

# Chapter 4

# Simulation of NEXAFS spectra

## 4.1 Computational Setup

For the simulation of NEXAFS spectra density functional self consistent field calculations were carried out using the WIEN2k [16] software package, which was already discussed in detail in the previous sections. The applied exchange correlation functional is the generalized gradient approximation (GGA) by Perdew, Burke and Ernzerhof (PBE) [15]. For the LAPW basis set $R \cdot K_{\max}$ was set to 6.0, which gives a corresponding plane wave cutoff energy of 19.8 Ry. The atomic sphere radii were set to 1.35 a.u. (0.714 Å) for boron and nitrogen and to 2.3 a.u. (1.217 Å) for nickel. For a proper simulation of a core hole the periodic cell of the *h*-BN/Ni(111) was expanded to a 2×2×1 supercell. By this scheme the atom with the core hole is surrounded by several atoms in the ground state so that hole-hole interactions are negligable and screening is also possible. In experimental NEXAFS spectroscopy on average only one of thousand atoms is excited during the experiment. The simulated cell contains boron nitride attached on both sides of a 19 layer nickel slab and a vacuum of approximately 30 a.u. (15.9 Å). The inversion symmetric

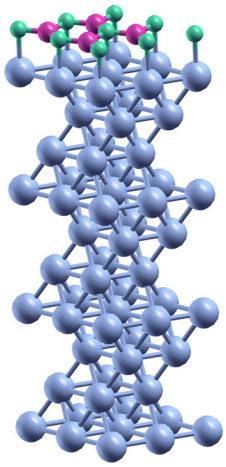

Figure 4.1: Ball and stick representation of the inversion symmetric part of the 2×2×1 *h*-BN/Ni(111) supercell with 19 nickel layers.

part of the cell is shown in figure 4.1. The presence of an inversion center reduces the computational effort since matrix elements become real instead of complex numbers, which leads to less memory consumption and requires less CPU time.

The geometric structure of a single layer *h*-BN grown on Ni(111) (for experiments see [47, 48, 49, 50]) was determined by DFT simulations [4], which showed that the nitrogen atoms are located directly on top of the nickel atoms of the last metal layer and the boron atoms are at the *fcc* hollow sites (appendix A.2 on page 106). The layer of *h*-BN is slightly buckled, with the boron atoms approximately 0.1 Å closer to the metal surface.

## 4.2 Spectra

### 4.2.1 Investigation of the core hole effect

For an accurate simulation of the X-ray absorption spectra it is necessary to investigate the influence of a core hole on the resulting spectra. According to Slater's *transition state theory* [44, 51] the best results are expected with calculations containing half a core hole. To carry out these simulations the occupation of the $1s$ orbitals of one of the boron or nitrogen atoms of the super cell was decreased by a half or one electron. The number of valence electrons was increased accordingly. For comparison also a calculation without a core hole was carried out. With these setups self consistend DFT calculations were performed and the corresponding spectra were simulated.

The resulting spectra are shown in figure 4.2 for the B-K (a) and the N-K (b) edge for the three different occupation numbers. The upper most curve shows the result for a full core hole, the middle one is obtained with half a core hole and the bottom curve without a core hole. It can be seen that the variation of the occupation number influences the resulting spectra especially in the region of lower photon energy (near the edge onset), where it has a significant effect on the relative intensity of the absorption maxima and their magnitude. For higher photon energies the effects get smaller but an influence remains. For boron the most significant effects appear between 190 eV and 202 eV. The first absorption maximum is strongly underestimated for the spectrum neglecting the core hole effect, whereas in the case of the full core hole additional features appear. From a direct comparison between the calculated and experimental spectra (figure 4.3) it can be seen that the simulations carried out with half a core hole show the best agreement, as was expected. Therefore all further simulations of NEXAFS spectra were carried

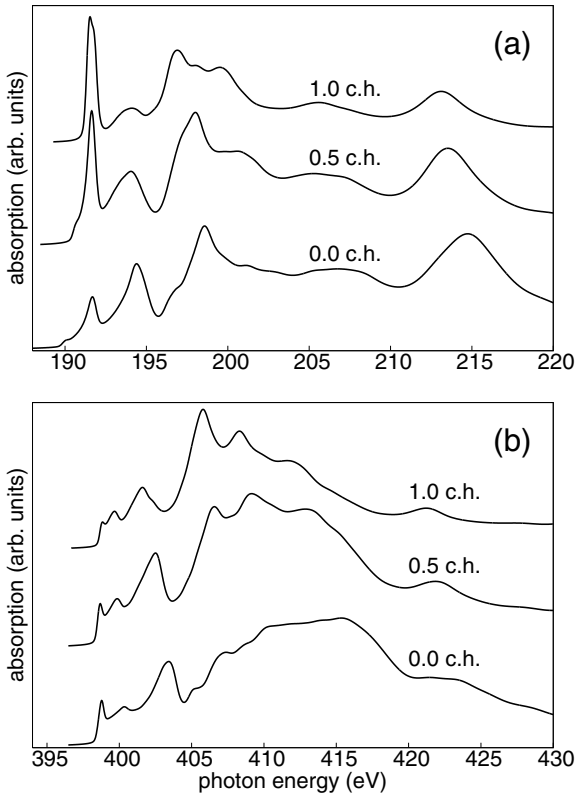


Figure 4.2: Simulation of core hole effects of X-ray absorption spectra of $h$-BN/Ni(111) for the B-K (a) and N-K (b) edge. The upper curve corresponds to a full core hole, the middle curve to half a core hole and the buttom curve shows the spectrum for no core hole.

out with this electronic configuration.

### 4.2.2 Simulation of Spectra

Simulations of NEXAFS spectra were carried out for the *h*-BN/Ni(111) and additionally for bulk *h*-BN to study the influence of the metal substrate and to gather information about bonding properties of the investigated system. In figure 4.3 a direct comparison of the simulated spectra with experimental data [3] is shown for bulk *h*-BN and the *h*-BN monolayer grown on the nickel surface. The solid lines represent the result of the calculations and the dashed lines the experimental spectra.

In both cases, the bulk and the surface system, the simulated spectra are in very good agreement with the experiment. The spectrum for the B-K edge (figure 4.3.a) shows a small discrepancy in the intensities for the first absorption maximum. However, different experimental data for *h*-BN bulk structures [52, 53, 54, 55, 56, 57, 58, 59] show that the observed intensities are very sensitive to the experimental setup. Especially the angle of incidence and the type of filtering yield large variations in the observed intensities. Additionally the broadening of the simulated spectra modifies sensitively the spectra particular at energies close to the absorption edge. Overall one can say that the experimental and simulated data are in quite good agreement. Besides the differences in the derived intensities just discussed, the energies of the absorption maxima and all other significant characteristics of the spectra can be reproduced.

The comparison between the bulk *h*-BN and the *h*-BN/Ni(111) spectra (figure 4.3.a) shows a significant difference, since in the latter case an additional small 'pre-peak' appears at approximately 191 eV as a result of the bonding to the Ni(111) surface. This additional absorption maximum is even

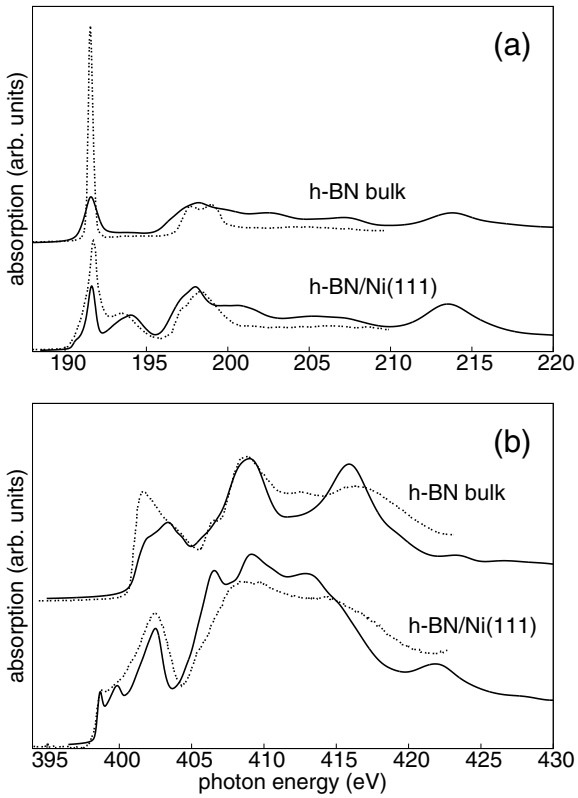


Figure 4.3: NEXAFS spectra of the B-K (a) and N-K (b) edge for the computationally derived data (solid line) assuming half a core hole in comparison with experimentally obtained spectra[3] (dashed lines).

more pronaunced for the N-K edge (figure 4.3.b) at approximately 398 eV, whereas the rest of the spectra is very similar.

Additionally a simulation of angle resolved spectra was carried out. This allows further insight how bonding occurs. Simulating an angle of incidence of 0 degrees corresponds to the $z$-oriented $p$ orbitals, while an angle of 90 degrees envolves the $x$- and $y$-oriented $p$ orbitals. Experimentally only spectra at an angle of incidence of 20 and 90 degrees are available. The resulting spectra are shown in figure 4.4.a for the B-K edge and figure 4.4.b for the N-K edge. The solid lines represent the simulated spectra and the dashed lines the experimental data [3]. Also in this case all spectra can be well reproduced and show that the characteristics in the lower energy region (190 eV to 196 eV for boron and 398 eV to 403 eV for nitrogen) derive from the transition of the $1s$ core electron to the $p_z$ orbitals ($\pi^\star$-bands), whereas at higher energies the transitions to the $p_x$ and $p_y$ orbitals ($\sigma^\star$-bands) are dominant. Some deviations in the low angle spectra can be explained by the 20 degree angle in the experimental setup.

## 4.3 Bonding Properties of *h*-BN/Ni(111)

In order to obtain a deeper understanding of the bonding properties between the $h$-BN layer and the Ni(111) surface the partial density of states (DOS) of the nitrogen $p$ and the nickel $d_{z^2}$ orbitals were analyzed, since these are the responsible orbitals for bonding. Due to the magnetic moment of the nickel surface a spin splitting occurs for the $h$-BN system. As shown in figure 4.5 there are two main regions for each spin, where a significant overlap of the corresponding partial DOS occurs. A part of the interaction takes place in the energy range marked in light blue from $-7.90$ eV up to $-4.10$ eV for spin

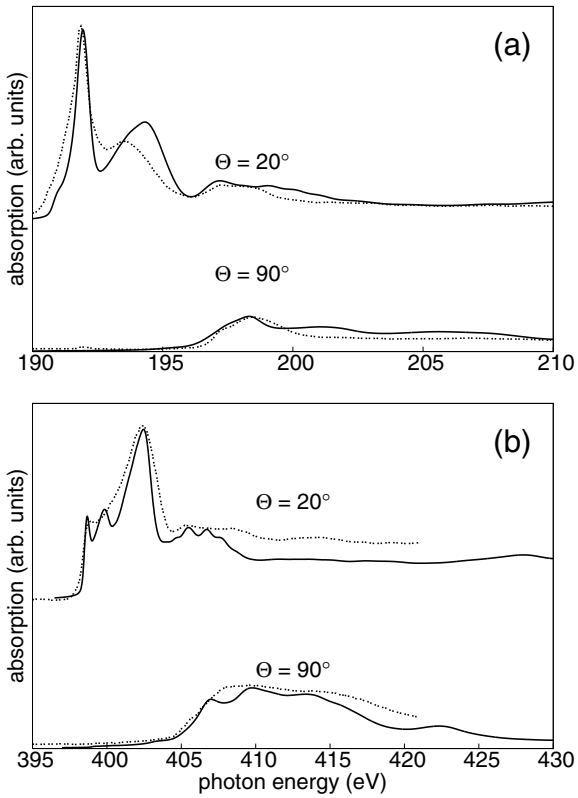


Figure 4.4: Angle dependency of NEXAFS spectra for the B-K (a) and N-K (b) edge for $h$-BN/Ni(111). Computational derived data are represented by the solid line and experimental data [3] by the dashed line.

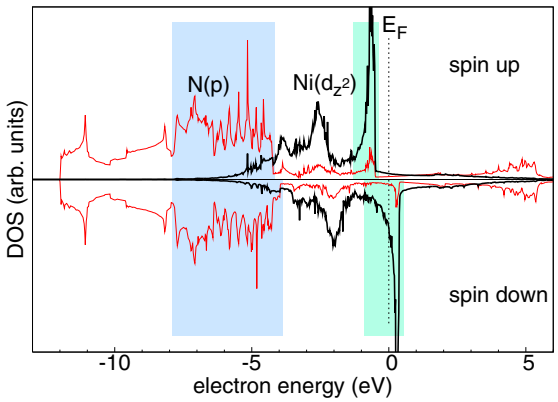


Figure 4.5: Partial DOS of N($p$) and Ni($d_{z^2}$) for $h$-BN/Ni(111). The colored areas show the regions of significant overlap of the N($p$) and Ni($d_{z^2}$) states.

up and $-3.77$ eV for spin down. The other overlap is present in the range from $-1.30$ eV to $-0.25$ eV for spin up and from $-0.67$ eV to 0.50 eV for spin down (marked in light green). For these energy ranges the electron densities are calculated within the Ni-B-N plane. The resulting electron densities of all four regions are shown in figure 4.6. The density plots for the low energy regions are very similar for spin up (a) and spin down (b) and differ only little. The scaling of the contour lines is exponentially with a factor of $\sqrt{2}$.

As expected there is a high electron density between the Ni atoms due to the metallic character. Furthermore a high density - indicating strong bonding character - is present between the nickel and the nitrogen atoms and the nitrogen and the boron atoms (N-B $\sigma$ bonds) respectively. This situation changes for the region of higher energies. In this case a significant difference is found between the corresponding densities for spin up and spin down electrons. What both densities have in common is the fact that - in contrast to the densities of the low energy regions - a very low density between nickel and nitrogen is present, which can be explained as an anti-

bonding interaction between nickel and nitrogen, where the corresponding wave functions have a node. The repulsion of the electrons can be well seen from the distortion of the nitrogen $p_z$ orbitals which have a far shorter extension towards the nickel atom as in the opposite direction (vacuum). Also in both cases a significant interaction of the boron $p$ orbitals with the nickel surface is present, which is still bonding (nodeless). The electron density plot for spin up shows a four center bonding (between three nickel and one boron atom) indicated by symmetry and the increase in electron density below boron with the contour line marked with 4.53 e·Å$^{-3}$.

It should be mentioned that for spin up electrons the electron density shown for both regions belong to states below the Fermi level and thus are occupied whereas for spin down electrons the states of the high energy region are mainly unoccupied. The increased density between boron and three nickel below is still present (figure 4.6.d) but smaller (contour 1.60 e·Å$^{-3}$), the corresponding electron density between the nickel atoms is also smaller. The electron density distribution between boron and nickel is only present in direction to the nearest (three) nickel atoms resulting in a distortion of the nickel states. These observations explain the observed buckling of the $h$-BN layer on the nickel surface, where the boron atoms are closer to the metal. On the one hand the $sp^2$ character of the $h$-BN is weakened due to bonding to the metal interface. On the other hand nitrogen shows bonding and anti-bonding states that are both occupied resulting in a weakening of the nitrogen nickel bond. For boron, however, mainly the bonding states are occupied which reveals - according to the electronic behavior discussed above - that the main bonding of the $h$-BN layer comes from the four center bond of boron in the $fcc$ sites of the nickel surface.

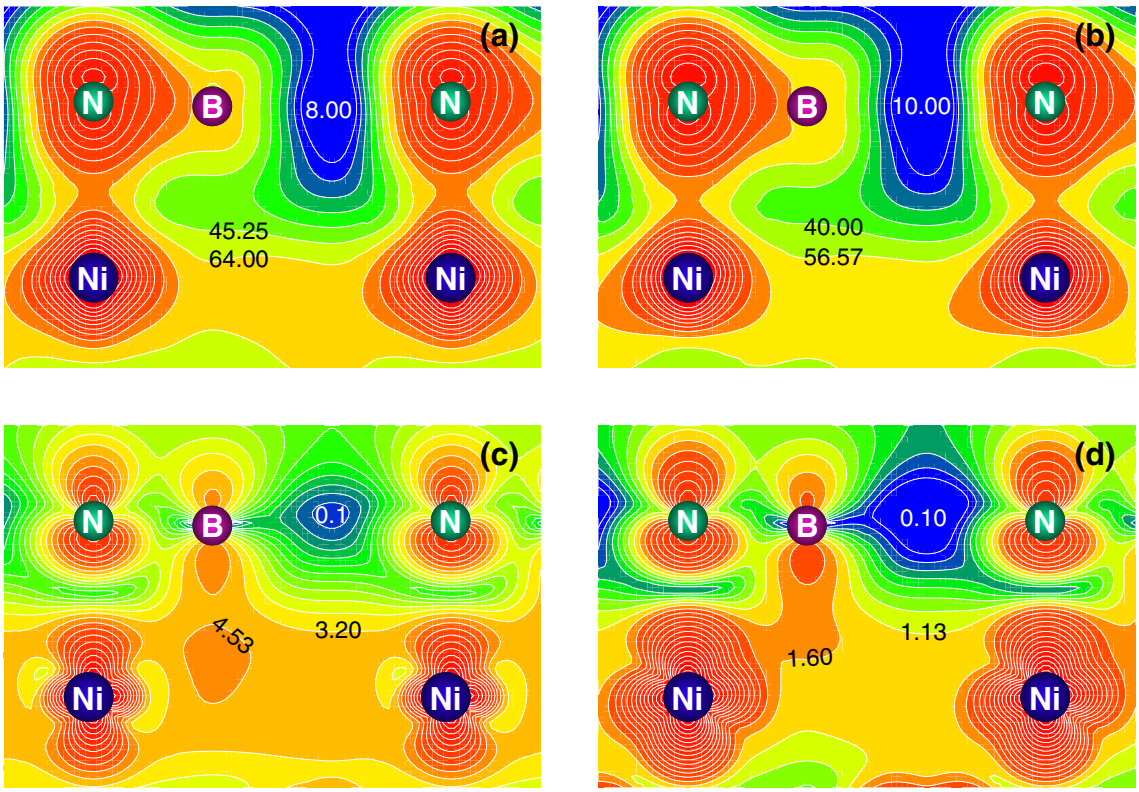


Figure 4.6: Electron densities in the Ni-B-N plane perpendicular to the Ni surface of the four energy regions shown in figure 4.5. The first row shows the electron density for spin up (a) and spin down (b) of the low energy regions whereas the second rows shows the density for spin up (c) and spin down (d) in the high energy regions. (Unit of contour values is e·Å$^{-3}$)

# Chapter 5

# *h*-BN/Rh(111)

## 5.1 Computational Setup

The simulations of the *h*-BN/Rh(111) system were carried out using the software package OpenMX [8] which is based on pseudopotentials and capable of O(N)-DFT calculations that allow a geometry optimization in a convenient time. In contrast to other software packages like SIESTA or CPMD it has the great advantage to be able to handle metallic systems, which is mandatory for the present case. In detail all calculations were carried out using an O(N)-DFT calculation based on a Krylov subspace algorithm [60, 22, 61]. For the exchange correlation potential the generalized gradient approximation (GGA) by Perdew, Burke and Ernzerhof (PBE) [15] was applied. The plane waves cutoff energy is set to 100 Hartree (200 Rydberg) and the basis sets consists of *s2p2d1* for Rh and *s2p2* for B and N (defining type and number of basis functions). The size of the truncated clusters within the O(N) scheme is defined by a *hopping range* of 15 Å and a *hopping number* of 2 (see chapter 2.2.2.2 on page 37 for details). The starting geometry for the structure optimization is a 12×12 Rh(111) super cell consisting of three

layers to simulate the metal substrate on which a 13×13 flat hexagonal boron nitride was placed (on one side). This leads to a hexagonal unit cell with a total of 770 atoms and unit cell vectors of 32.16 Å in $x$- and $y$-direction and 37.04 Å in the $z$-direction. The geometry of the Rh slab is taken from the optimized structure of Rh bulk obtained by DFT calculations with WIEN2k. The initial geometry is shown in figure 5.1. To avoid any interaction of the $h$-BN/Rh(111) with its periodic image (due to the periodic boundary conditions) a vacuum of approximately 30 Å is introduced, which causes the large lattice spacing along the $z$ direction. For a stable solution of the self consistent calculation, which is crucial for metallic systems, the mixing scheme by Kerker [62] is applied. The pseudopotentials [19, 63] are taken from the OpenMX homepage [8] without modifications. The bulk metal substrate had to be approximated by just three layers, since this is the maximum that can be handled by the available computational resources. The geometry of the first two rhodium layers is kept fixed and only the third rhodium layer, which is in contact with $h$-BN and the boron nitride layer itself is allowed to relax. For further details the input file of the calculation is listed in the appendix B.1.1 on page 108. The computational resources used for this calculation were 32 dual CPU nodes (Sun X4100, 2 dual core AMD Opteron 275 2.4 GHz, 8 GB RAM and 70 GB HDD) connected via Fast Ethernet and low-latency Infiniband for MPI calculations. Due to the demand of memory (about 6 GB per MPI job) only one CPU per node could be used. With the described setup the complete geometry relaxation took about 40 days of computing time.

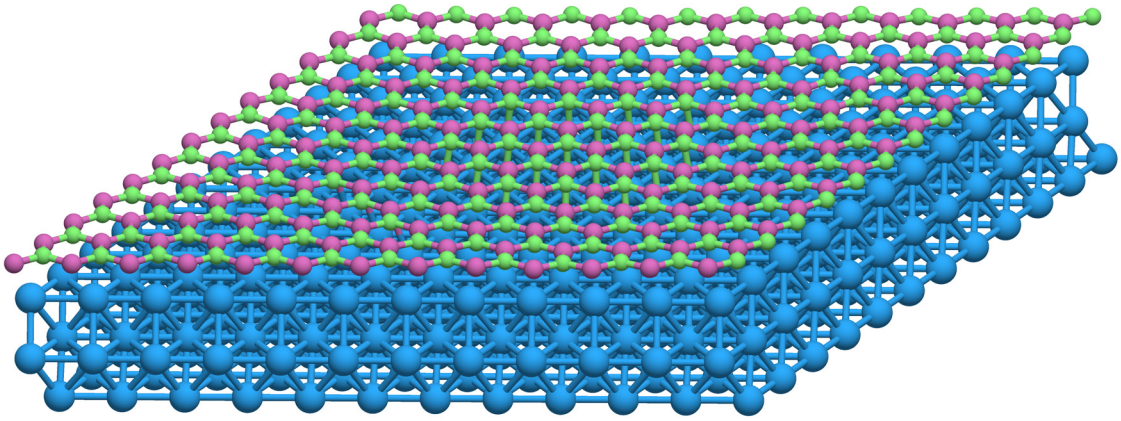

Figure 5.1: The initial structure of the hexagonal supercell consisting of three layers of 12×12 Rh(111) and one layer of 13×13 *h*-BN. The blue balls represent the rhodium atoms and the red and green balls boron and nitrogen respectively.

## 5.2 Geometric Structure

### 5.2.1 Relaxation of the *h*-BN Layer

The geometry of the initial cell (figure 5.1) was relaxed till the resulting forces were below a threshold (0.01 Hartree/Bohr) and thus the positions of all atoms did not change significantly between the optimization steps. The optimization resulted in a corrugation of the *h*-BN layer of up to 0.85 Å around an average distance to the topmost Rh layer of 2.46 Å (table 5.1). The topology of the relaxed structure is shown in figure 5.2. The relative height of *h*-BN above the top Rh layer (i.e. the *z*-coordinate) is shown by color coding (blue to magenta: *low*; red to yellow: *high*). An approximately spherical *low* region (i.e. a short rhodium boron-nitride distance) is surrounded by *wires* (*high* regions) with a much larger rhodium boron-nitrogen distance.

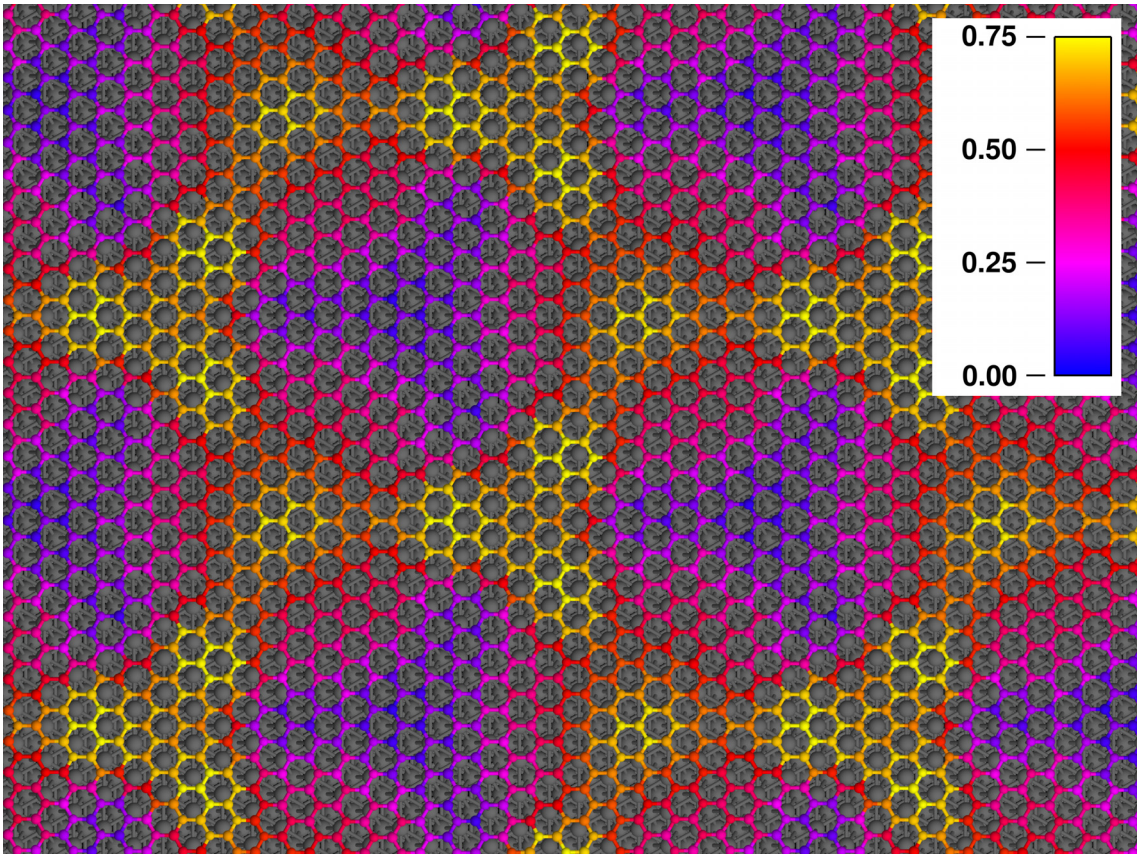


Figure 5.2: Corrugation of the *h*-BN layer on the Rh(111) surface forming a nanomesh. The Rh atoms beneath the *h*-BN layer are shown in gray, the lower regions of boron and nitrogen are marked in blue, violent and magenta, whereas the atoms in the higher positions are colored in red, orange and yellow.

The *low* region (for a detailed view see figure 5.3) has a diameter of approximately 20 Å and forms an additional threefold "flower" like corrugation, which is rather small in comparison to the overall corrugation. This region also clearly shows the buckling of boron and nitrogen atoms similar to the epitaxial structure of *h*-BN/Ni(111) with the boron atoms closer to the metal than the nitrogen atoms. As discussed in the previous section this indicates that also in this system the bonding between metal and the *h*-BN layer is dominated by boron-metal multi-center bonds. This is also confirmed by the geometric situation. In the *low* regions the boron atoms are situated in or near to the *fcc* position (appendix A.2 on site 106) with respect to the metal slab but nitrogen atoms are at or near to the on-top position of the metal layer.

At the border of the *low* region the boron-nitrogen height changes rather abruptly and leads to regions that are further away from the metal (*high* regions). The highest part (shown in yellow) has a threefold symmetry (figure 5.4) and is rather flat. A more detailed investigation of this high region shows its highest positions at its vertices with a small well in the middle. In the three highest positions the boron atoms are situated near to the highest rhodium atoms while nitrogen is above the metal atoms of the second layer, which seems to be the driving force for the high spacing. In the well (which is just marginally closer to the metal) that is in the middle of the three maxima the three boron atoms are exactly in the *hcp* and the three nitrogen atoms in the *fcc* sites with respect to the metal surface. Although the bonding situation is much weaker the buckling of boron and nitrogen can still be observed.

The third region to mention is again a high region (figure 5.5). In comparison to the other high regions already described above it is smaller with

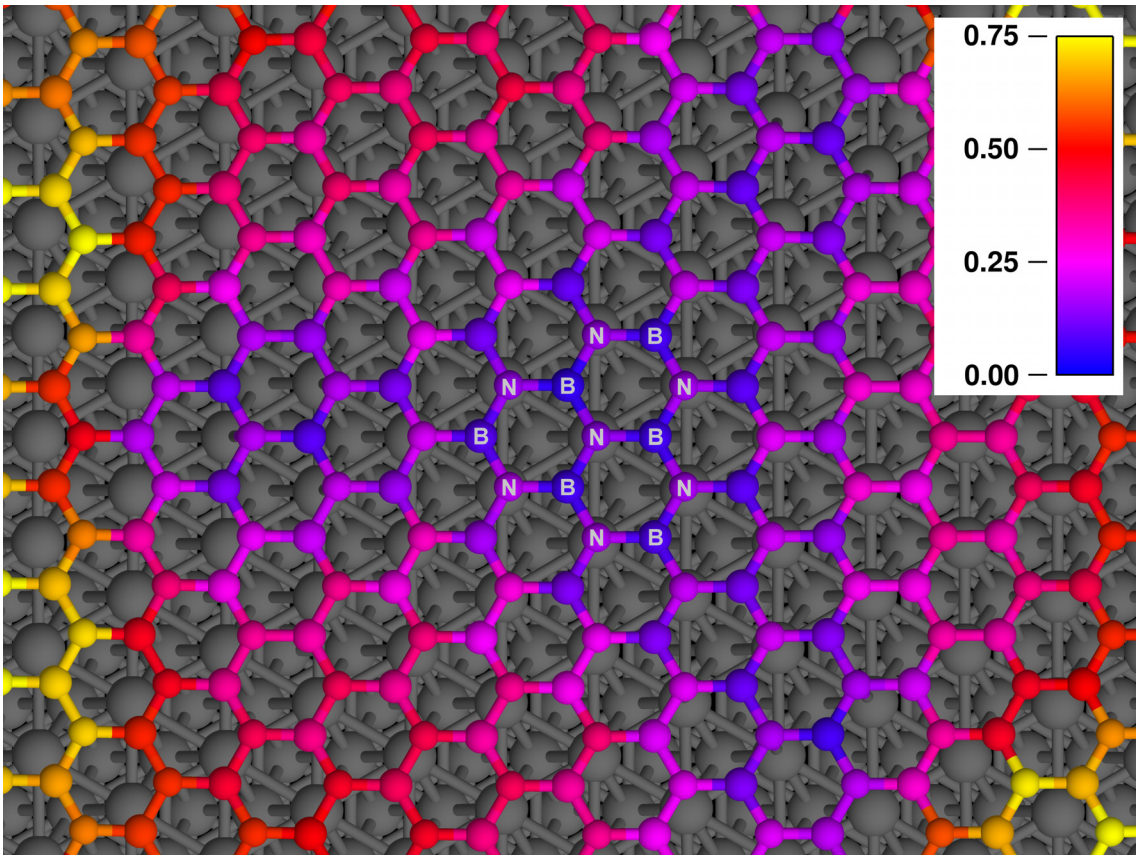


Figure 5.3: Detailed *h*-BN/Rh(111) nanomesh topology of the *low* region. This area is indicated by the blue to red coloring of the *h*-BN layer, with the nearly flat triangle in the middle that also shows the buckling of the layer. In this energetically favourable situation the boron atoms are close to the *fcc* and the nitrogen atoms to the *on-top* positions.

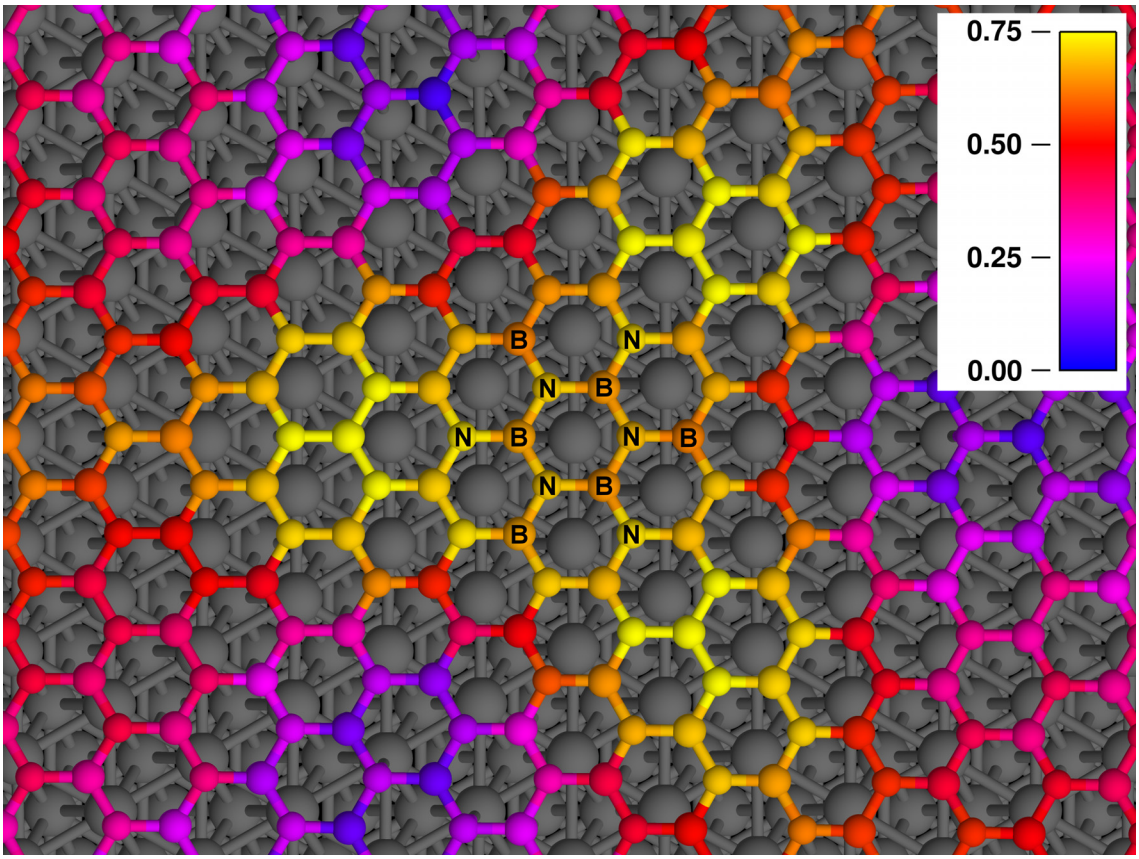


Figure 5.4: Detailed *h*-BN/Rh(111) nanomesh topology of the *high* region 1. It shows a triangular shape with the boron atoms in or near *hcp* and the nitrogen atoms in *fcc* position.

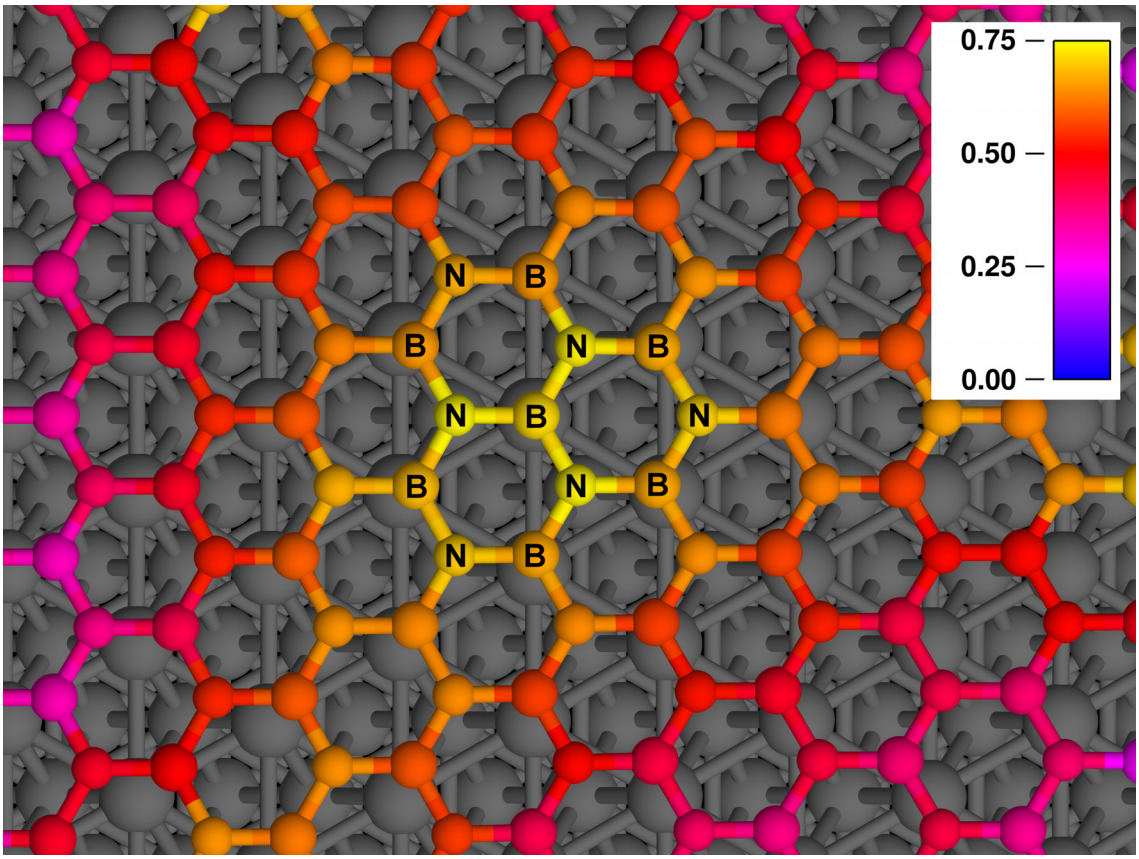


Figure 5.5: Detailed *h*-BN/Rh(111) nanomesh topology of the *high* region 2. Here the are the boron atoms in *on-top* position and the nitrogen atoms in *hcp* position.

about 6 Å in diameter. Here the highest position is reached where one boron atom is in the on-top position of rhodium and nitrogens are at the *hcp* sites. In combination the higher positions form a honeycomb like structure with the *low* region as the hole in the middle. This is qualitatively in good accord with the STM images [5] shown in figure 1.1 on page 13. Also the experimentally derived corrugation of approximately 0.1 nm is in very good agreement with the theoretical value of 0.085 nm. The calculated relaxed structure yields an average buckling of *h*-BN, where the boron atoms are in average 0.15 Å closer to the metal surface than the nitrogen atoms. This is in good agreement with the results obtained for *h*-BN/Ni(111) where a buckling of 0.1 Å was observed [4].

In the meantime the structure was also investigated using the WIEN2k package [64, 65], which became feasible due to a newly implemented iterative diagonalization algorithm. The structure obtained by the first WIEN2k calculations [64] is shown in figure 5.6. A comparison of the geometry optimizations by OpenMX and WIEN2k show the same characteristics besides a few small differences. Note that OpenMX uses PBE, but WIEN2k the new exchange correlation functional by Wu and Cohen [66], which may be responsible for this deviation.

The main differences to the structure obtained with OpenMX are that the *low* region, which is larger in the calculation with WIEN2k, has a nearly hexagonal (instead of trigonal) form and the *high* regions which are split into an intermediate region and high spots. The first high region discussed for the OpenMX calculation (figure 5.4) is rather flat and about 0.2 Å lower than the highest region, which correspond to the high region 2 from OpenMX (figure 5.5). The spacing between metal and the boron nitride layer is approximately the same for both *high* regions. Other small differences between the two

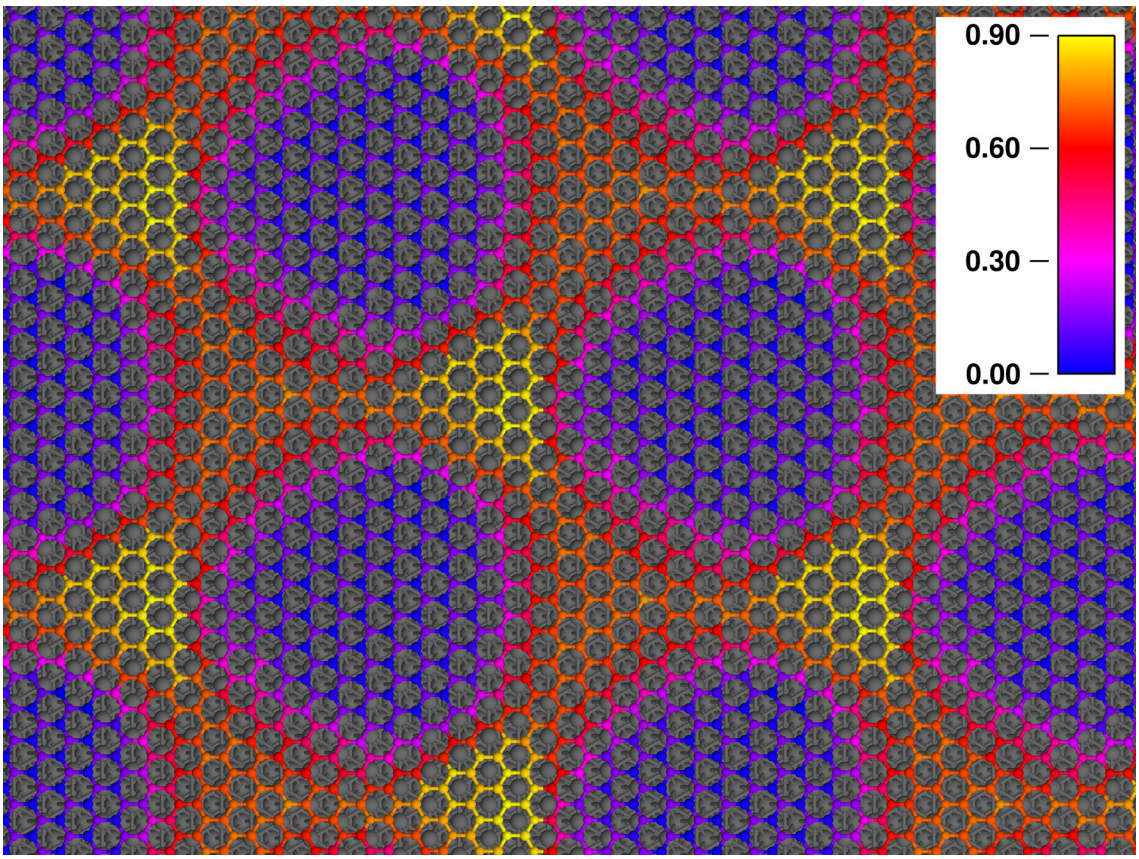


Figure 5.6: *h*-BN/Rh(111) nanomesh topology calculated with WIEN2k [64]. The large spherical *low* region is shown in blue and magenta. The *wires* are formed by the *higher* regions shown in orange and yellow.

calculated structures are in the corrugation and average spacing. WIEN2k shows - in contrast to the values from OpenMX - an overall corrugation of 0.92 Å , which is 0.08 Å larger, and an average spacing of 2.56 Å, which is 0.10 Å larger (table 5.1) than for OpenMX. The buckling of boron and nitrogen atoms is also present in the WIEN2k calculations and best observed in the low region but the overall buckling with just 0.07 Å is smaller by a factor of two.

| | OpenMX | WIEN2k |
|---|---|---|
| max. corrugation BN-layer | 0.85 Å | 0.92 Å |
| max. corrugation Rh-layer | 0.21 Å | 0.05 Å |
| max. B-Rh dist. | 2.91 Å | 3.02 Å |
| min. B-Rh dist. | 2.06 Å | 2.14 Å |
| max. N-Rh dist. | 2.91 Å | 3.07 Å |
| min. N-Rh dist. | 2.15 Å | 2.27 Å |
| avg. BN-Rh dist. | 2.46 Å | 2.56 Å |

Table 5.1: Data of the relaxed $h$-BN/Rh(111) nanomesh

New results obtained with WIEN2k [65] show a considerably larger corrugation of approximately 1.9 Å. Although the same *ab initio* approach was used in both calculations the previous geometry optimization was stopped after the forces had dropped below a threshold of 0.005 Hartree/bohr. It was found that the BN-layer in the nonbonding regions appears to be extremely flexible in the direction perpendicular to the metal surface. Thus the remaining small forces show a significant influence on the BN-metal distance in those regions and therefore affect the geometry optimization significantly. Due to the fact that the applied threshold for the OpenMX calculations was set to 0.01 Hartree/bohr the influence of these small forces was disregarded.

### 5.2.2 Relaxation of the Rh Surface

A further point of interest of the geometry relaxation is the behavior of the metal surface. The calculation with OpenMX shows that the Rh atoms are qualitatively corrugated in the same way as the $h$-BN layer. This means that

the metal atoms are "following" the relaxed $h$-BN surface with respect to the z-axis, but with a much smaller value. The OpenMX calculation revealed a corrugation for the metal layer of 0.21 Å, which is smaller by a factor of four than the boron nitride corrugation. The results from WIEN2k yield a much smaller displacement along the $z$-axis of only 0.045 Å. Experimental values about the corrugation of the metal layers are not yet available.

# Chapter 6

# *h*-BN/Pt(111) 9/10-Cell

## 6.1 Computational Setup

In analogy to the calculation of the *h*-BN/Rh(111) system the calculation on Pt(111) was carried out using OpenMX with the Krylov subspace algorithm to achieve a reasonable fast geometry optimization. The applied exchange correlation potential was again GGA-PBE and the plane waves cutoff energy was set to 100 Hartree (200 Rydberg). The original pseudopotentials were used without any modifications and the basis sets were *s2p2* for boron and nitrogen and *s2ps2d1* for platinum. The same procedures as in the previous calculation were applied, which is 15 Å for the *hopping range* and 2 for the *hopping number*. Also for this system the Kerker mixing scheme [62] was applied.

The starting geometry for this calculation is a 9×9 Pt(111) super cell with three layers and a flat *h*-BN layer that is placed on top of the platinum slab. For this system the boron nitride layer forms a 10×10 unit cell to match the Pt(111) lattice spacing. In this case the lattice mismatch reaches already a value of 10.8 %. The geometric parameters of the hexagonal cell are

therefore 25.01 Å for the $a$- and $b$-directions and 50.00 Å for the $c$-parameter to introduce a large vacuum to avoid interaction with the periodic image. The initial cell is shown in figure 6.1 and has a total number of 443 atoms. Also in this case the structure of the Pt cell is based on the DFT optimization by WIEN2k for the bulk system. For all details the input file for the calculation can be found in the appendix B.1.2 on page 111.

In contrast to the simulation of the nanomesh formed on Rh(111) first only the boron and nitrogen atoms were allowed to relax and all metal atoms were kept fixed. After the geometry of the $h$-BN layer was optimized, also the platinum layer in contact with the boron nitride was allowed to relax. The calculation was carried out on an IBM 1350 cluster (IBM x335, 2 Pentium Xeon IV Nocona 3.6 GHz, 4 GB RAM and 80 GB HDD) using 32 dual CPU nodes. Again, due to the memory demand of the calculation, only one CPU per node could be used. However, since the platinum system is smaller - in contrast to $h$-BN/Rh(111) - nodes with 4 GB memory were sufficient and it was possible to take advantage of the faster CPUs. The overall computing time to fully relax the geometric structure was about 30 days.

## 6.2 Geometric Structure

### 6.2.1 Relaxation of the $h$-BN Layer

The atomic positions were optimized in two steps, first with the topmost metal layer fixed and than relaxed together with the boron nitride till the forces nearly vanished.

The resulting structure showed a large overall corrugation of the $h$-BN layer of 1.78 Å with an average spacing to the platinum layer of 3.03 Å (table 6.1). The obtained structure is shown in figure 6.2, where the $z$-positions

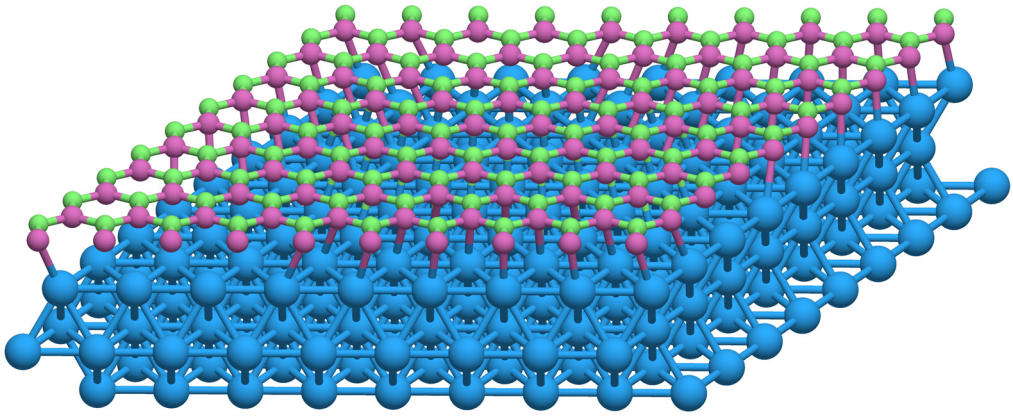

Figure 6.1: The initial structure of the hexagonal supercell consisting of three layers of 9×9 Pt(111) and one layer of 10×10 *h*-BN. The large blue balls represent the platinum atoms, the red and green balls the boron and nitrogen atoms.

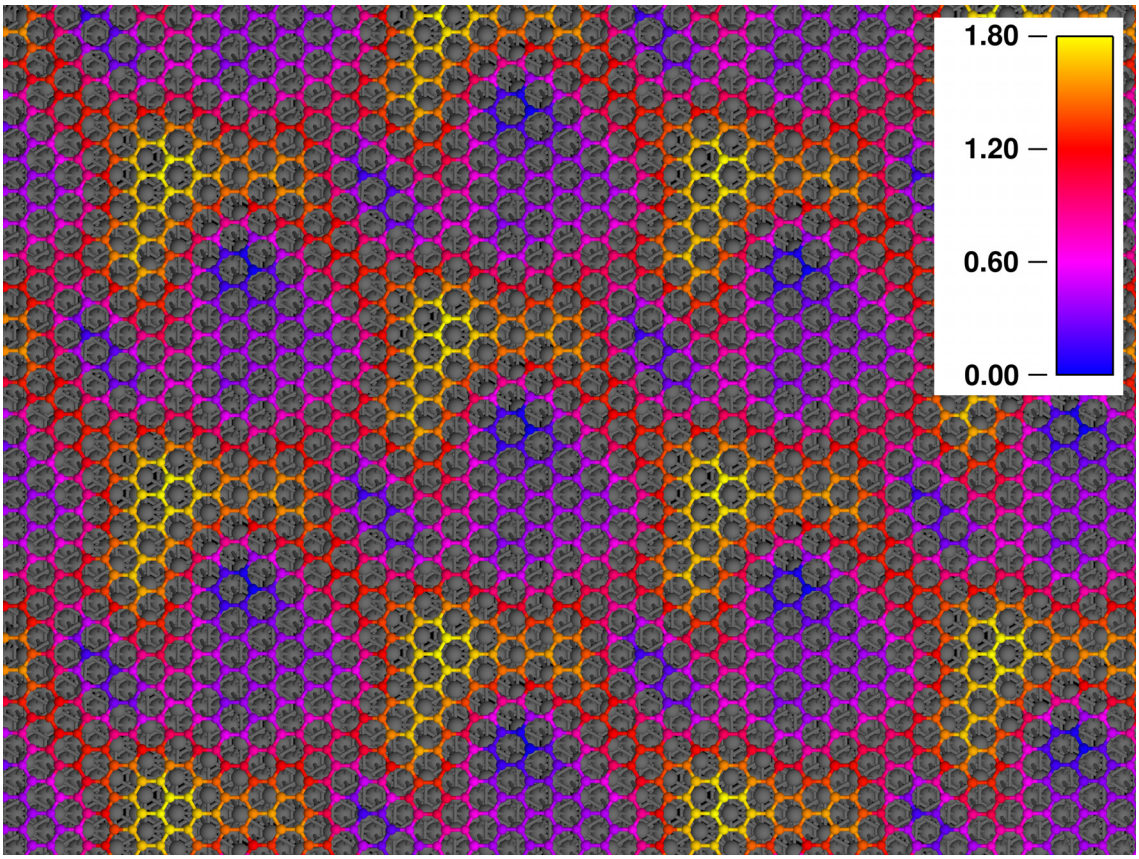


Figure 6.2: *h*-BN/Pt(111) nanomesh topology. The platinum layers are colored in gray and for boron and nitrogen lower positions are shown in blue and violet and *high* positions in red and yellow.

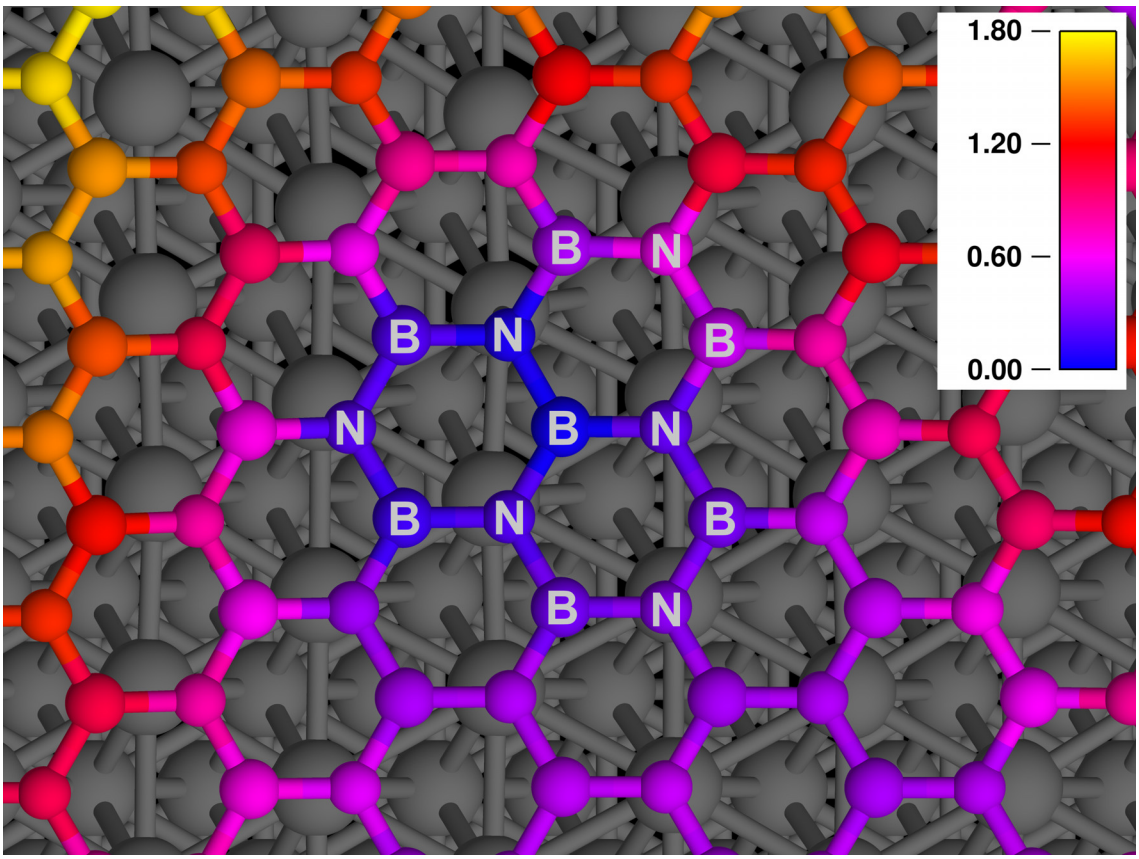


Figure 6.3: *h*-BN/Pt(111) nanomesh topology of low region 1. The boron atoms are close to the *fcc* postion and the nitrogen atoms nearly *on-top*.

of the atoms are color coded. In comparison to the nanomesh formed on Rh(111) the situation has changed completely. The *low* region with a maximum diameter of approximately 6 Å is a little bit pear-shaped. This region, which is shown in detail in figure 6.3, has the closest boron nitride spacing to platinum when the boron atoms are near to the *fcc* sites with respect to the Pt(111) and the nitrogen are near on-top of the metal layer. This is exactly the configuration that was found to be most stable for *h*-BN/Ni(111) and *h*-BN/Rh(111) and thus has again the strongest attraction between the

metal and the boron nitride.

As a result of the large lattice mismatch of 10.8 % the geometrical situation changes rapidly from one metal atom to the next, and thus the region of strong bonding is rather small. This results in a non flat geometry for the low region, so the overall changes with respect to the $z$-coordinate are rather smooth. A further consequence of the permanently changing geometry (and thus bonding quality) is the large region of intermediate height. Another region, where the geometric arrangement between $h$-BN and Pt is similar, is a large area of approximately 8 Å where the boron atoms are situated in or near the *hcp* sites and the nitrogens at *fcc* positions. Due to this energetically unfavorable (bonding) configuration a region with a high spacing to the metal surface (figure 6.4) is formed.

The next region with a significant change in height is shown in figure 6.5. In this situation the boron atoms are in on-top position with respect to the highest platinum layer and the nitrogen atoms are situated at the *hcp* sites. However in contrast to the expected repulsion this is one of the regions of closest spacing. For the $h$-BN/Ni(111) the corresponding configuration has been reported to be unstable [4] and in the calculation of $h$-BN/Rh(111) it results in a region of large spacing (figure 5.5). It is very unlikely that this results from different physical properties between nickel, rhodium and platinum. A comparison with the optimized geometry obtained with WIEN2k and experimental data suggest that for this system OpenMX seems to fail to predict the proper structure.

### 6.2.2 Relaxation of the Pt Surface

The relaxation of the Pt surface behaves similarly to the one obtained for $h$-BN/Rh(111). Also in this case the atomic positions of platinum follow the

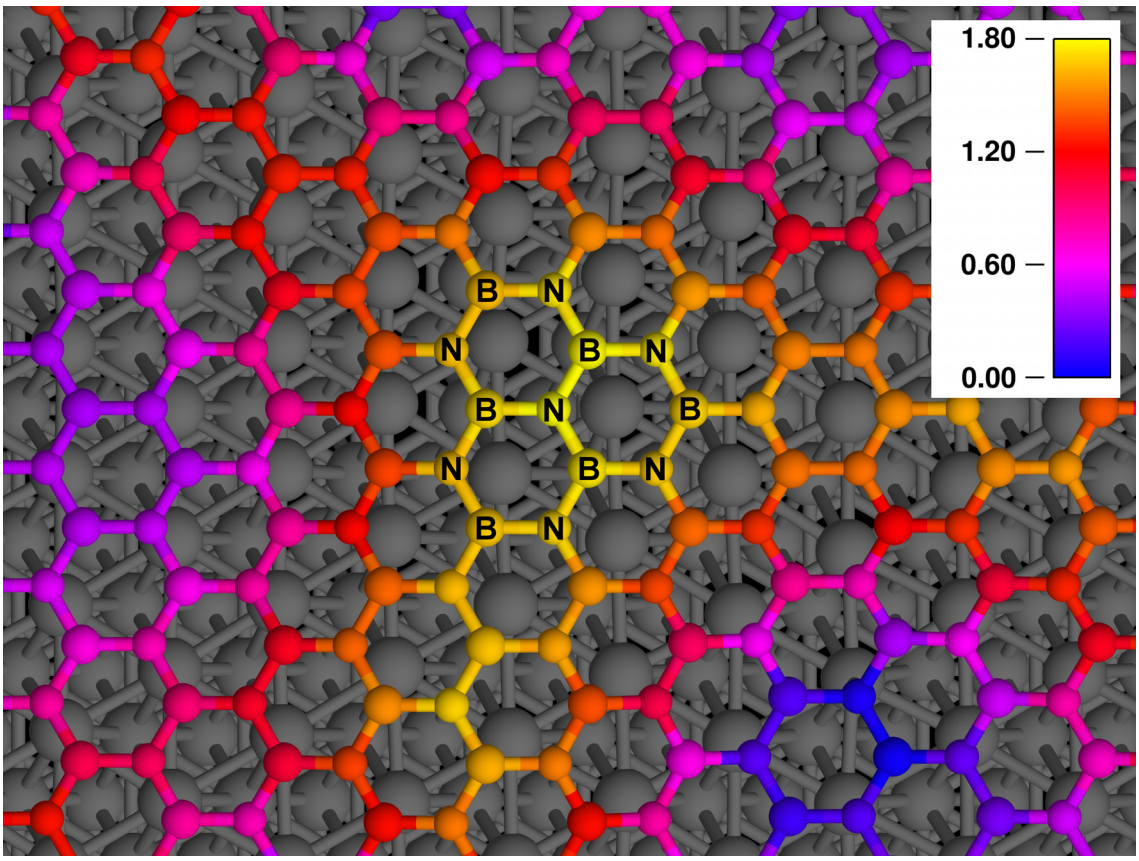


Figure 6.4: *h*-BN/Pt(111) nanomesh topology of the high region. The boron atoms are close to *hcp* and the nitrogen atoms near the *fcc* positions.

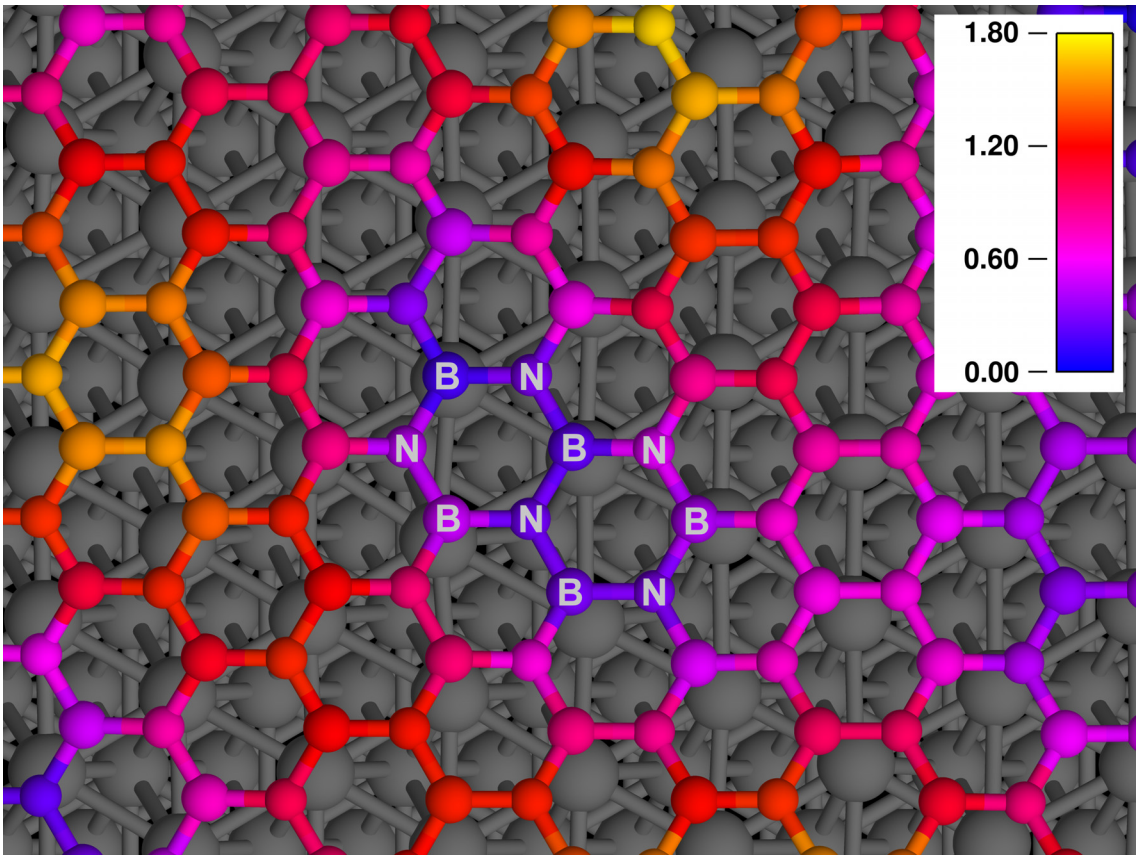


Figure 6.5: *h*-BN/Pt(111) nanomesh topology of the low region 2. Although the boron atoms are in *on-top* position and the nitrogen atoms in the *hcp* sites, which should be energetically unfavourable, a close spacing is obtained.

characteristics of the *h*-BN layer with respect to the *z*-coordinate. An overall corrugation of the top Pt(111) layer of 0.42 Å is found with OpenMX. In comparison to the rhodium nanomesh this is twice as much. The increase of the average spacing between the Pt(111) layers is 0.08 Å. With WIEN2k no relaxation of the reacting Pt layer was carried out, since only very small forces occur so that a corrugation of less than 0.05 Å is expected. Of course this is also in contrast to the results obtained with OpenMX.

### 6.2.3 Comparison with Experiment and with WIEN2k

The results obtained from the calculations with OpenMX are compared to the experimental data [67] and a DFT calculation carried out by WIEN2k. Unfortunately the assumption that this simulation is not as accurate as for the *h*-BN/Rh(111) is confirmed. The geometry relaxation carried out by WIEN2k resulted in a much smaller corrugation for the boron nitride interface of only 0.53 Å in contrast to 1.78 Å. Also the average spacing between metal and interface is about 8 % smaller with 2.79 Å instead of 3.03 Å (table 6.1). Not only the values for the corrugation and spacing are different but also the topology shows other characteristics. The topology derived by WIEN2k is shown in figure 6.6. In this case the low region has the form of a triangle with chopped vertices with a size of approximately 10 Å in diameter. The deepest location within this area is located near one edge and is similar to the result obtained with OpenMX, i.e. where the boron atoms are placed close to the *fcc* sites and the nitrogen atoms in on-top position. Also the highest regions qualitatively correlate with the results from OpenMX with boron in *hcp* and nitrogen in *fcc* position.

The questionable second low region, with boron at the on-top position and nitrogen in *hcp* configuration derived by OpenMX can not be reproduced

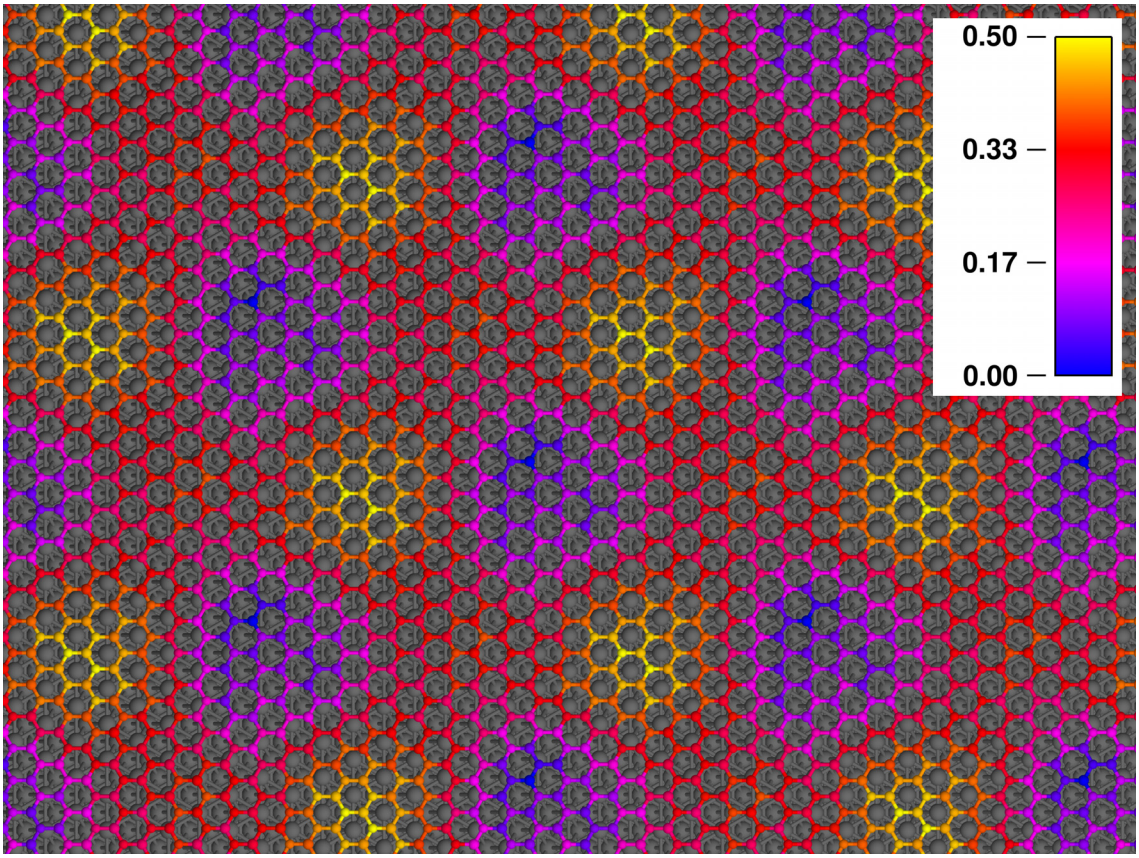


Figure 6.6: *h*-BN/Pt(111) topology calculated with WIEN2k.

| | OpenMX | WIEN2k |
|---|---|---|
| max. corrugation BN-layer | 1.78 Å | 0.53 Å |
| max. corrugation Pt-layer | 0.42 Å | 0.00 Å |
| max. B-Pt dist. | 3.88 Å | 2.98 Å |
| min. B-Pt dist. | 2.12 Å | 2.51 Å |
| max. N-Pt dist. | 3.90 Å | 3.04 Å |
| min. N-Pt dist. | 2.15 Å | 2.56 Å |
| avg. BN-Pt dist. | 3.03 Å | 2.79 Å |

Table 6.1: Data of the relaxed $h$-BN/Pt(111) nanomesh

with WIEN2k. Here the region is part of a large intermediate area. Of course this has a large effect on the topology and explains why the two structures look qualitatively so different (figure 5.2 and 6.6).

According to experimental data obtained by Preobrajenski et al. [67] the STM image (figure 6.7) shows a topology much more like the one derived from WIEN2k and further suggests only a slight corrugation across the supercell which is in contradiction to the obtained 1.78 Å and also favors the WIEN2k result. Recent calculations carried out with WIEN2k [65], which apply a lower threshold for the remaining forces, confirm the obtained corrugation of 0.5 Å.

### 6.2.4 Problems of the OpenMX Calculations

According to the previous discussion the possible reason for the inaccurate OpenMX calculation has to be determined. An error within the program itself is very unlikely otherwise also the calculation of the rhodium system

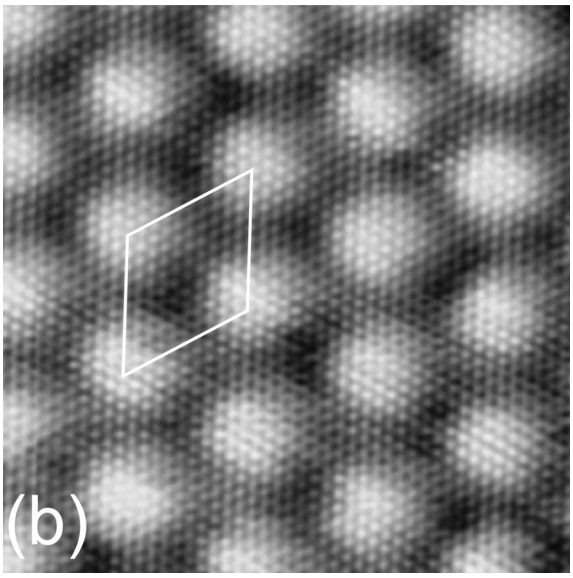


Figure 6.7: STM image of the Pt(9/10) nanomesh [67]. The white rhomb indicates the unit cell.

should have been problematic. Due to the fact that the program is based on pseudopotentials and atomic basis sets, the change from one system to another may cause problems since the quality of the potentials and the applied basis set may be atom dependend. In contrast to OpenMX, WIEN2k is an all electron full potential code, which does not depend on any sort of predefined atomic data and thus makes the change from one element to another more reliable.

The pseudopotentials used are the ones provided [19, 63] by the author of OpenMX, who tested and further checked them against the data from NIST [68]. Therefore the possibility that an improper pseudopotential has been used seems to be rather unlikely. One point that has a significant influence on the quality of the calculation is the applied basis set. For all calculations within this thesis the minimal configuration for the metal atoms had to be

used to reduce the memory demand and the corresponding CPU time. While this setup was obviously sufficient for the rhodium system it failed for the platinum system.

A small test calculation has been carried out to check this assumption. A 1×1 cell of 7 Pt(111) layers and epitaxially *h*-BN layers at both sides of the surfaces was set up. In order to eliminate any effect resulting from the use of different exchange correlation potentials, similar calculations were carried out using GGA-PBE for both WIEN2k and OpenMX. In the case of the WIEN2k calculation the platinum slab (7 layers) showed an expansion of 0.05 Å in thickness with respect to the optimized bulk structure. In the case of the OpenMX calculation a much larger increase of 1.06 Å was found. The spacing between the metal and boron nitride of 2.46 Å for WIEN2k is also in contrast to 3.40 Å obtained by OpenMX. Further the direct comparison of the platinum bulk unit cell optimization shows that OpenMX leads to a 2 % (0.08 Å) larger lattice parameter compared to WIEN2k. An enhanced basis set for platinum (*s2p2d2f1*) for the OpenMX calculation showed an expansion of the metal slab of 0.78 Å which is 26 % less than for the standard setup. Since this is an indication that a larger basis set would improve the calcuation for the *h*-BN/Pt(111) nanomesh the additional computational effort would be higher than for the WIEN2k calculation and thus not resonable.

Another point that could play a role for the nanomesh structure is that in OpenMX and WIEN2k different exchange correlation potentials were used for the relaxation. As already mentioned OpenMX uses the generalized gradient approximation by Perdew, Burke and Ernzerhof [15] but in the WIEN2k calculation a new GGA potential by Wu and Cohen [66] was applied. The GGA-PBE potential is known to generally underestimate bonding characteristics while the new potential by Wu and Cohen provides more accurate

solutions [66], which might play an important role in the weak bonding that takes place between $h$-BN layer and the metal.

# Chapter 7

# Borazine on Rh(111)

To be able to study the formation of the nanomesh on different metal surfaces it is important to understand the influence of the metal on the bonding characteristics of the precursor forming the *h*-BN layer. The precursor, that was mainly used to form the different meshes is borazine [5] (see chapter 7.1 for details). For the formation of the *h*-BN layer three possible approaches can be considered.

The first reaction path that could form the layer is a splitting of borazine into single B-N species which recombine on the surface afterwards. A second possibility is that a ring opening of the precursor occurs and a reaction between those fragements takes place. The third alternative is the direct combination of borazine rings by hydrogen eliminiation. It should be mentioned that the formation of the *h*-BN layer could be observed also with a chloro substitued derivative of borazine (Trichloroborazine) but it was not yet possibe to achive the reaction with precursors without a preformed six ring (and $sp^2$ bonding).

Within this chapter the interaction between borazine and the Rh(111) surface will be discussed, which was the first system where the nanomesh

was observed and which is also investigated most [5, 7].

## 7.1 Free Borazine Molecule

Theoretical investigations of borazine were carried out to determine the necessary energy for hydrogen cleavage from the molecule, which is the mandatory step to enable a further - not yet fully known - recombination resulting in the regular *h*-BN layer. Borazine shows very similar characteristics in comparison to benzene. It is isostructural and also isoelectronic, except that boron and nitrogen show different electron negativities which results in polar character and a higher localization of the electrons. For this similarity to benzene borazine is also called *inorganic benzene*. However borazine shows a much smaller thermal stability (it decomposes easily and releases $H_2$) and is far more reactive due to the polarized bond between nitrogen and boron.

Ab inito calculations were carried out to determine the energies that would be necessary to achieve a separation of a single hydrogen atom from the molecule (in the gas phase). This was carried out by stepwise removal of a hydrogen atom from the molecule performing a spin polarized calculation to be able to simulate the radical. These calculations were carried out for both cases, the cleavage of a hydrogen from a boron or a nitrogen atom, respectively. The results for the calculation are listed in table 7.1. As shown the cleavage of the boron-hydrogen bond is energetically more favorable than breaking the nitrogen-hydrogen bond. Also molecular dynamics calculations showed that the energy, which is necessary to achieve a cleavage (of an isolated molecule) is very high, and so it is very unlikely that it occurs in the gas phase at about 1000 Kelvin.

Due to the ultra high vacuum (UHV) in the experiments the interac-

tion between two borazine molecules in gas phase is considered as negligible. Therefore the formation of a reactive compound is expected to take place at the interface with the metal as a catalyst lowering kinetic barriers.

## 7.2 Adsorbed Borazine

This section deals with the basic characteristics of borazine in contact with the metal interface. The aim of the first part of the investigation was to determine the position of borazine on the interface that is energetically most stable.

Ab intio calculations were carried out on a 6×6 Rh(111) supercell consisting of three metal layers and an additional single borazine molecule. The energetically stable positions for the borazin molecule were determined by geometry optimization. According to these calculations the most favorable position is present when the boron atoms are placed in the *fcc* sites relative to rhodium and nitrogen on top of the rhodium atoms of the uppermost interface layer (figure 7.1). This is in good agreement with the structure of the *h*-BN/Rh(111) nanomesh where the corresponding geometric configuration is also the most stable one.

Furthermore the calculations showed a metastable configuration with the boron atoms in the *hcp* sites. A configuration where boron is placed on top of the rhodium is not stable and relaxes immediately to one of the two described configurations above. This is also in agreement with the structure of the rhodium nanomesh, since this unstable case is exactly the configuration where the highest spacing between *h*-BN mesh and rhodium substrate occurs. (For details on the *h*-BN/Rh(111) nanomesh see chapter 5 on page 61.)

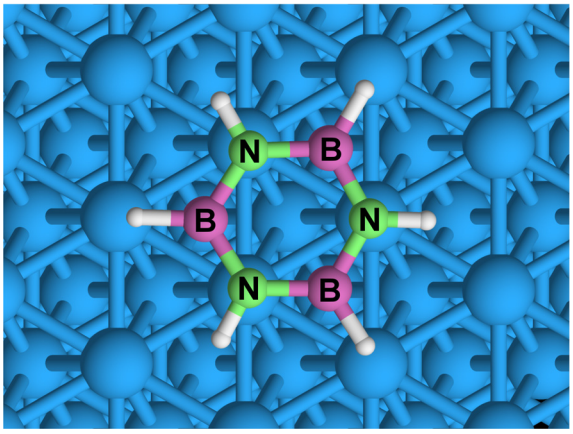


Figure 7.1: Most stable position of borazine on Rh(111)

### 7.2.1 Adsorption Energy

As discussed in the previous sections the thermal stability of borazine is still high and therefore a decomposition of the molecule in the gas phase is very unlikely. Due to the ultra high vacuum when the reaction is carried out, and borazine being the only reactant, a reaction between two molecules or another substance in the gas phase can be neglected. Following these considerations the reaction has to take place on the metal surface. Therefore in this section the effect of the metal on the borazine molecule and its bonding properties are investigated.

The first interesting question is how strong borazine is bonded to the metal surface. DFT calculations were carried out to explore the energy dependence with respect to the metal molecule distance. The results are shown in figure 7.2, with an energy minimum at the most stable distance at 2.27 Å. It shows a bonding energy of about 256.68 kJ·mol$^{-1}$. The calculations were carried out for the optimal (lateral) positions of borazine with respect to the metal surface. The obtained value shows the highest bonding energy at the

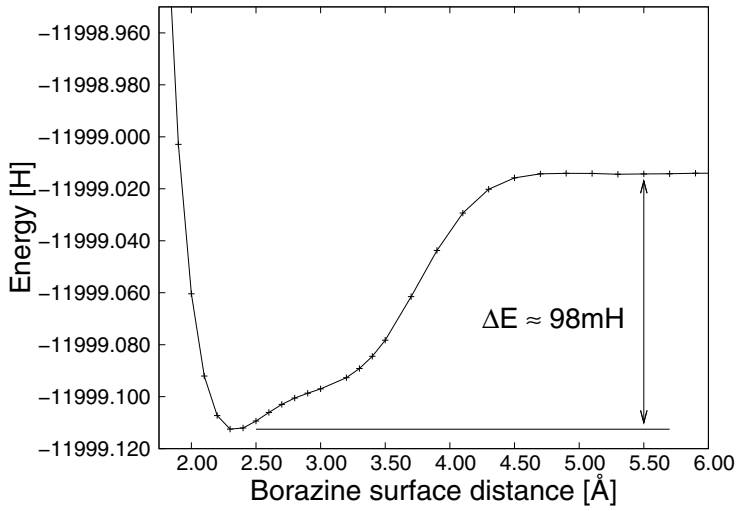


Figure 7.2: Energies for adsorption of borazine

most favourable adsorption site. According to the previous section a different position of borazine above the rhodium surface would result in reduced bonding or even unbound states. An interesting detail that can be observed for the bonded borazine is the result that the initially planar structure of the free borazine gets lost. The hydrogen bonds are bent upwards (in the $z$-direction), with an angle of approximately 12 degrees out of plane (0.24 Å). Also the ring molecules shows a small corrugation of 0.06 Å, with the boron atoms closer to the metal surface. These are significant indicators that the bonding within the molecule is weakened and thus a cleavage of a hydrogen atom becomes energetically more favorable.

### 7.2.2 Hydrogen cleavage of adsorbed borazine

In this section the necessary energy for the separation of a hydrogen atom from the borazine molecule, which is adsorbed on the Rh(111) layer, will be determined. In two types of calculations the hydrogen bond to either a

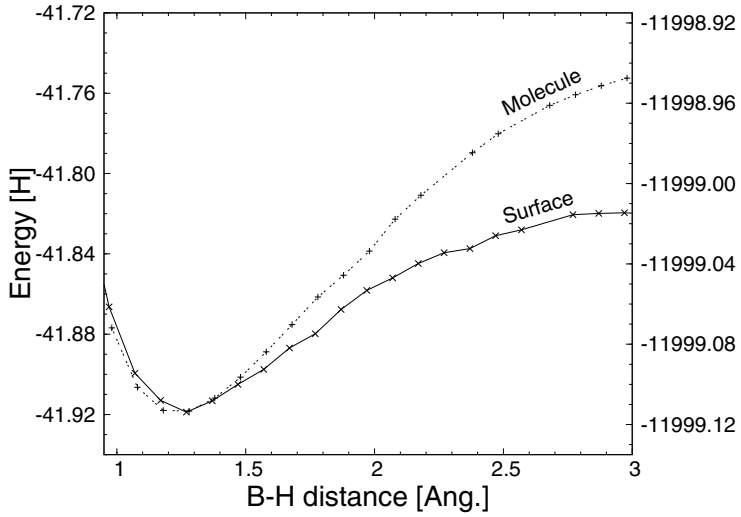


Figure 7.3: Energies for cleavage of the B-H bond at the rhodium surface in comparison to the isolated molecule.

boron or a nitrogen atom was elongated stepwise and the resulting energy was calculated, which allowed to estimate the energy for the complete removal of a hydrogen atom. The resulting energy curves varying the bond length in the range of 1 to 3 Å are shown in figure 7.3 for boron and in figure 7.4 for nitrogen. It can be seen that the presence of the metal is significant and the energy curve is lowered with respect to the free molecule already at small distances, especially for nitrogen. The extrapolated energies are presented in table 7.1 with the interesting result that the metal borazine interaction significantly reduces the nitrogen hydrogen bond to 225.59 kJ·mol$^{-1}$ and the boron hydrogen bond to 260.49 kJ·mol$^{-1}$. With respect to the gas phase this is a decrease in bonding energy of 32 percent for the boron hydrogen and nearly 61 percent for the nigrogen hydrogen bond.

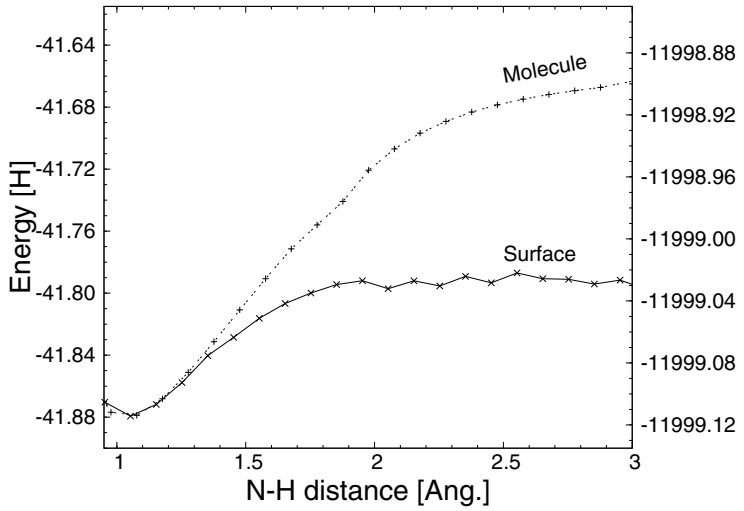


Figure 7.4: Energies for cleavage of the N-H bond at the rhodium surface in comparison to the isolated molecule.

| | $E_{\text{Cleavage}}$ free borazine | | $E_{\text{Cleavage}}$ adsorbed borazine | |
|---|---|---|---|---|
| Bond | [mH] | [kJ·mol$^{-1}$] | [mH] | [kJ·mol$^{-1}$] |
| B-H | 146.3 | 383.98 | 103.1 | 260.49 |
| N-H | 218.6 | 573.90 | 89.3 | 225.59 |

Table 7.1: Energies for B-H and N-H cleavages of free and adsorbed borazine.

## 7.3 Formation of the *h*-BN layer

The aim of this section is to develop a possible reaction path that explains how the hexagonal boron nitride mesh is formed from single borazine molecules. In general there exist three plausible reactions that would allow to generate the *h*-BN monolayer. The first one is that the borazine molecule decomposes completely into B-N fragments that reassemble again on the surface and form the *h*-BN. Similar to this is the consideration that a ring opening of the precursor molecule occurs and those larger fragments recombine. What makes these approaches unlikely is that a cleavage of the borazine ring has to take place in both cases. Even though the polarized bonds make borazine more reactive than benzene, the ring structure is still very stable. Preliminary molecular dynamics calculations (just for a few ps) showed that borazine does not break quickly at temperatures up to 3000 K, even in contact with the metal surface. In addition it seems unlikely that highly reactive B-N fragments would form such a regular and ordered structure without any side reactions, for example forming cubic boron-nitrogen (*c*-BN). Especially the latter agrument is a strong indication for the direct reaction of borazine rings. Due to the four-fold coordination in *c*-BN this modification is energetically more stable than the three-fold coordination of *h*-BN. In contrast to graphene borazine is the metastable configuration.

The third reaction that could take place is a recombination of two complete borazine rings by simple hydrogen elimination. This would explain how and why such a well defined structure is formed. To initiate this step hydrogen has to be split off from a borazine ring which either recombines with another borazine radical or is able to propagate a further elimination.

The calculations in the previous section showed that the cleavage of a boron hydrogen or a nitrogen hydrogen bond is possible with moderate energy

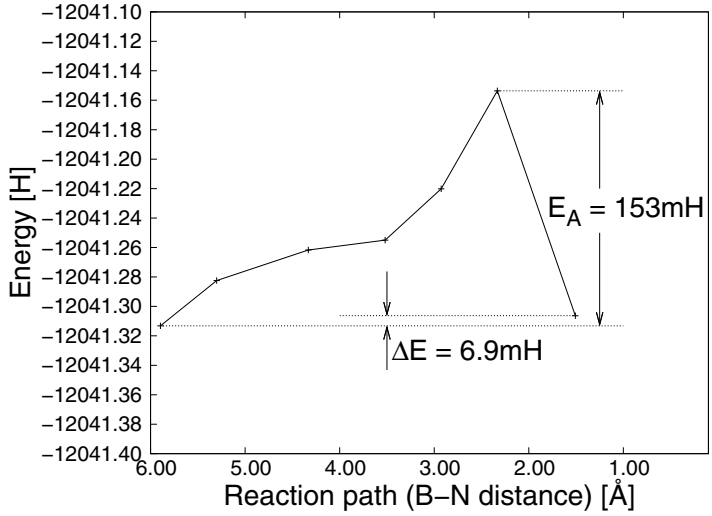


Figure 7.5: Reaction path for the combination of two borazine rings by hydrogen elimination. The activation energy $E_A$ is about 135 mH and the reaction energy is 6.9 mH.

if the borazine is in contact with the metal surface. Assuming that the reaction takes place only if both reaction partners are on the surface the energetic demand to overcome the kinetic barrier can be calculated by moving the molecules continuously closer until a reaction takes place.

This calculation was carried out on a 6×6 supercell of Rh(111) consisting of 3 layers. One borazine was placed in the optimal position and a second molecule was constrained to move closer. The two rings were oriented in such a way that the corners of rings move towards each other. To achieve a realistic energy estimation only the position of one boron and one nitrogen atom were constrained. All other positions were allowed to relax. The results of these calculations, which are shown in figure 7.5, indicate that an energy barrier of approximately 400 kJ·mol$^{-1}$ has to be overcome to achieve a reaction. The resulting structure of the two borazine rings connected by one boron nitrogen

bond is only by 18 kJ·mol$^{-1}$ less favorable than the two free borazines, which is energetically nearly equal. It should be mentioned that in this calculation the borazine rings were fully saturated and the cleavage of hydrogen was achieved by the short distance of the reacting boron nitrogen pair. The energy calculated by this reaction path should therefore be the maximum energy needed to achieve such a reaction. Taking the previous section into account one can note that the energy obtained by the absorbance of the borazine ring on the surface is already sufficient to cause a splitting of the nitrogen hydrogen bond and is very close to the energy for the boron hydrogen bond.

Considering the further reactions of the eliminated hydrogen atoms, which stay adsorbed on the surface, the necessary energy performing the hydrogen cleavage may even be less. During geometry optimization it could be observed that the free hydrogen atom underwent a reaction with the already combined borazine molecules. This resulted in a hydrogen elimination (by forming $H_2$) and consecutively the formation of a radical position on the borazine dimer. The energy gain for the formation of $H_2$ on the rhodium surface is 99.7 kJ·mol$^{-1}$.

Taking these facts into account the formation of the hexagonal boron nitride layer could be a radical chain reaction. In this case the calculated activation energy $E_A$ would only be necessary to initiate the first step. For the progagating steps the formation of $H_2$ is energetically favourable. Since the reaction is carried out under vacuum the formed hydrogen molecules are removed immediately from the equilibrium and the reaction is additionally shifted towards the boron nitride layer. The energy necessary for the desorption of the hydrogen molecule is determined to be 78.95 kJ·mol$^{-1}$.

# Part V

# Conclusions

# Electronic structure of *h*-BN/Ni(111)

In this thesis is was possible to characterize the electronic configuration of the epitaxially *h*-BN/Ni(111) system. The most stable configuration, which was determined in a previous work [3], was calculated using the software package WIEN2k. In accordance to *Slaters final state rule* the NEXAFS spectra for this structure were simulated by introducing a core hole for the exited atom. To avoid self-interactions of the exited atom (in reality only a very low fraction of atoms is exited simultaniously) it was placed within a supercell. The computated results were compared to experiment which showed good agreement for all spectra.

Additionally the electron densities were derived for several energy ranges, which are significant for bonding. This allowed to determine the bonding properties. It could be shown that not the expected rhodium-nitrogen bond but a multi-center rhodium-boron bond is responsible for the stability of the system. The reason for the repelling forces between nickel and nitrogen are the (partial) occupied nickel $d_{z^2}$ and nitrogen $p_z$ antibonding orbitals.

Due to the epitaxial growth of the *h*-BN mono-layer (with respect to the metal(111) surface), this system could be calculated with high precision but still reasonable computing time, because of the small unit cell. It showed

to be a good reference model for the *nanomesh* systems, which are formed on other transition metals like Rh(111) and Pt(111) but are much more expensive in computational resources.

# Geometry Optimization with OpenMX

In this work the geometry optimizations for the one layer model [7] of the nanomeshes ($h$-BN/Rh(111) and $h$-BN/Pt(111)) were carried out using the software package OpenMX. This program was used because of the large unit cells, which contain almost one thousand atoms. In contrast to conventional DFT methods it allows calculations with a linear scaling with respect to the system size (number of atoms) and therefore a significant reduction of computational resources.

Later during this work it became feasible to carry out these calculations also with WIEN2k, which allowed to investigate the quality of the results obtained by the O(N) method in detail.

## 9.1 $h$-BN/Rh(111)

For the case of the $h$-BN/Rh(111) system the geometry optimization resulted in partial agreement with experiment and the WIEN2k calculations.

While the calculated corrugation showed the same characteristics as the STM images, the maximum difference in the metal $h$-BN distance of 0.85 Å is greatly underestimated. The value obtained by WIEN2k calculations is

1.9 Å. This is caused by the extreme flexibility of the nonbonding areas where small forces show significant influence on the BN-metal distance. Since the applied force threshold for geometry optimization with OpenMX was set to 0.01 Hartree/bohr this effect was disregarded. Furthermore the geometries obtained by OpenMX and WIEN2k show differences in the shape of the *h*-BN layer. The buckling of the *h*-BN layer, with the boron atoms in average 0.15 Å closer to the metal surface than the nitrogen atoms, was also observed for the WIEN2k calculation but with a smaller value of only 0.07 Å.

A further disagreement was found for the corrugation of the metal surface. While OpenMX and WIEN2k showed the same characteristics, namely that the atoms of the metal layers shift accordingly to the displacement of the boron-nitride layer, OpenMX obtained a much (nearly five times) larger corrugation of 0.21Å.

## 9.2 *h*-BN/Pt(111)

The OpenMX calculation of the *h*-BN/Pt(111) system failed partly. Although the calculation still showed a corrugation the characteristic features could not be reproduced, neither those of experiment nor those of the WIEN2k calculation. While the WIEN2k calculation gave an overall corrugation of 0.53 Å, which is consistent with the experiment, a much larger result of 1.78 Å was obtained by the OpenMX calculation. Also the corrugation of the top platinum layer was significantly overestimated with 0.42 Å, which is expected to be smaller than 0.05 Å. The reason therefore is mainly found in an insufficient basis set. Test calculations showed that a better basis set would improve the results but is computationally too demanding for the large nanomesh cell.

## 9.3 Formation of the *h*-BN mono layer

The adsorption properties of borazine on the Rh(111) surface were investigated and a possible reaction path for the formation of the *h*-BN monolayer was studied. It could be shown that the adsorption of borazine to the metal surface significantly reduces the stability of the boron-hydrogen and nitrogen-hydrogen bonds. In detail the energies, which are necessary for hydrogen elimination, were determined with 260.49 kJ·mol$^{-1}$ for the boron-hydrogen (free molecule: 573.90 kJ·mol$^{-1}$) and 225.59 kJ·mol$^{-1}$ for the nitrogen-hydrogen bond (free molecule: 383.98 kJ·mol$^{-1}$).

According to experimental results and theoretical considerations the formation of the *h*-BN layer by recombination of borazine rings, with concomitant hydrogen elimination, was determined as the most probable reaction and therefore investigated in detail. The reaction of single B-N fragments or larger molecules obtained by ring cleavage are expected to be energetically less feasible, which is supported by the fact that until now the *h*-BN layer could only be formed in experiment by precursors that are borazine derivatives.

Ab initio calculations were carried out to determine the reaction properties between two borazine rings adsorbed to the Rh(111) surface. The results indicate that an activation energy of approximately 400 kJ·mol$^{-1}$ is necessary to achieve a reaction, which results in a structure of two borazine rings connected by one boron-nitrogen bond. The resulting dimer is only 18 kJ·mol$^{-1}$ less stable than the two adsorbed borazine rings but additional energy can be gained by the formation of $H_2$ (99.7 kJ·mol$^{-1}$) on the metal surface.

# Part VI

# Appendix

# Appendix A

# Geometric Structure

## A.1 Face Centered Cubic Geometry

There exist two possibilities to achieve a *closed sphere packing*, where the only difference is in the stacking sequence. The *hexagonal close packed* structure (*hcp*) consists of two alternating layers (along the $z$-axis) of the same structure that are shifted by $(\frac{1}{3},\frac{2}{3})$ against each other. Therefore the atoms of the third plane are exactly above the atoms of the first one (figure A.1), which is called A-B stacking.

For the *face centered cubic* structure the third layer is again shifted by $(\frac{1}{3},\frac{2}{3})$, with respect to the previous two, resulting in a sequence of three different planes, that is denoted as A-B-C stacking. In figure A.1 the three different positions of the displaced layers are indicated by the use of different colors (blue, red, green). In this case the atoms of the fourth layer (which is not shown in the figure) are again above those of the first plane.

The layers forming the stacking correspond to the (111) planes for the *fcc* structure and to the (001) planes for *hcp* system.

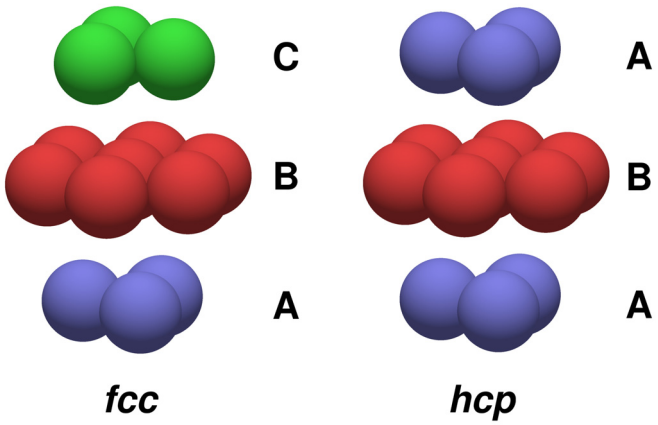


Figure A.1: Comparison between *face centered cubic* (*fcc*) and *hexagonal closed package* (*hcp*) structures. The *fcc* structure has an A-B-C stacking (blue, red, green) and the *hcp* structure an A-B stacking (blue, red) of the atomic metal layers with respect to the crystallographic (111) direction for *fcc* and (001) direction for *hcp* geometry.

## A.2 Geometry of *h*-BN/Me(111)

The *h*-BN/Me(111) systems, which are discussed in this thesis, consist of a hexagonal boron-nitride (*h*-BN) mono-layer above a (111) metal surface. The investigated metals crystallize in the *fcc* structure, resultinq in sequence of tree geometrically different layers perpendicular to the (111)-surface (A-B-C stacking). A geometric model is shown in figure A.2.

The large balls represent the metal atoms of the first four surface layers and the small gray balls show the optimum positions for boron (lightgray) and nitrogen (darkgray). The A-B-C stacking of the atomic layers (in (111) direction) of the metal is indicated by the large balls of different colors (blue, red, green). The boron and nitrogen atoms are shown in their energetically most favorable position with nitrogen *on-top* of the last metal layer (blue) and boron above the metal atoms of the after next layer (red). With respect to the geometry of the metal the boron atoms are in exactly the same position as the metal atoms of an additional layer, forming a *fcc* like geometry and thus the boron atoms are said to be in the *fcc*-position. If the vacant position above the atoms of the second metal in the boron-nitride layer would be occupied this would result in a *hcp*-like geometry (figure A.1) and therefore defined as *hcp*-position.

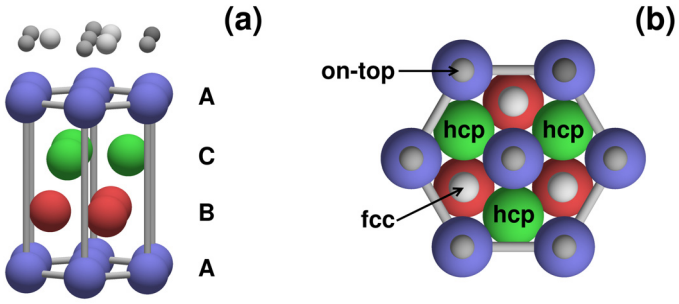


Figure A.2: Geometry of the $h$-BN/Me(111) system: The large balls represent the metal atoms of the first four surface layers and the small gray balls show the positions for boron (lightgray) and nitrogen (darkgray). A representative cell in side view is shown in figure (a) and the top view in figure (b) with the different atomic positions of the $h$-BN layer with respect to the metal surface.

# Appendix B

# Input Files

## B.1 OpenMX

### B.1.1 Rh Nanomesh

```
#      File Name
System.CurrrentDirectory          ./    # default=./
System.Name                      rhbn_on
level.of.stdout                   1    # default=1 (1-3)
level.of.fileout                  1    # default=1 (0-2)

# Definition of Atomic Species
Species.Number       3
<Definition.of.Atomic.Species
 Rh   Rh5.0-s2p2d1    Rh_GGA
 B    B5.0-s2p2       B_TM_PCC
 N    N4.0-s2p2       N_TM_PCC
Definition.of.Atomic.Species>

# Atoms
Atoms.Number         770
Atoms.SpeciesAndCoordinates.Unit   Ang # Ang|AU

Atoms.UnitVectors.Unit             Ang #  Ang|AU
<Atoms.UnitVectors                     # unit=Ang.
```

```
   27.8504694117  -16.0794760118    0.0000000000
    0.0000000000   32.1589520236    0.0000000000
    0.0000000000    0.0000000000   37.0423900000
Atoms.UnitVectors>

#Atom-Coordinates
#Atom#   Atom           xyz-Coordinates      el. Configuration
<Atoms.SpeciesAndCoordinates           # Unit=Ang.
      1   N    0.005840   -0.003500    9.747360    2.5  2.5
      2   N    0.000570    2.498310    9.760920    2.5  2.5
      3   N    0.000220    4.996750    9.765410    2.5  2.5
[...]
    169   N   -2.158230   -1.255920    9.758220    2.5  2.5
    170   B    1.442470    0.000360    9.684680    1.5  1.5
    171   B    1.437210    2.496290    9.662950    1.5  1.5
[...]
    338   B   -0.717380   -1.254950    9.673480    1.5  1.5
    339  Rh   -0.056260    0.000380    7.478480    8.5  8.5
    340  Rh   -0.061460    2.681100    7.498010    8.5  8.5
[...]
    768  Rh   -0.886160   -6.697950    3.196120    8.5  8.5
    769  Rh   -0.886160   -4.018040    3.196120    8.5  8.5
    770  Rh   -0.886160   -1.338130    3.196120    8.5  8.5
Atoms.SpeciesAndCoordinates>

# SCF or Electronic System
scf.XcType                  GGA-PBE     # LDA|LSDA-CA|LSDA-PW|GGA-PBE
scf.SpinPolarization        Off         # On|Off|NC
scf.partialCoreCorrection   Off         # On|Off
scf.ElectronicTemperature   2500.0      # default=300 (K)
scf.energycutoff            200         # (Ry)
scf.maxIter                 2000        # default=40
scf.EigenvalueSolver        Krylov      # DC|GDC|Cluster|Band
scf.Kgrid                   1 1 1       # means 4x4x4
scf.Mixing.Type             Kerker      # Rmm-Diisk
scf.Init.Mixing.Weight      0.0080      # default=0.30
scf.Min.Mixing.Weight       0.0010      # default=0.001
scf.Max.Mixing.Weight       0.0600      # default=0.40
scf.Mixing.History          5           # default=5
scf.Mixing.StartPulay       30          # default=6
scf.Kerker.factor           0.7         # default=1.0
```

```
scf.criterion               1.0e-3      # default=1.0e-6 (Hartree)

# 1D FFT
1DFFT.NumGridK              900         # default=900
1DFFT.NumGridR              900         # default=900
1DFFT.EnergyCutoff          3000

# Orbital Optimization
orbitalOpt.Method           Off         # Off|Unrestricted|Restricted

# output of contracted orbitals
CntOrb.fileout              off         # on|off, default=off

# SCF Order-N
orderN.HoppingRanges        15.0        # default=5.0 (Ang)
orderN.NumHoppings          2           # default=2

# MD or Geometry Optimization
MD.Type                     DIIS        # Nomd|Opt|NVE|NVT_VS|NVT_NH
MD.Fixed.XYZ                On
MD.Opt.DIIS.History         2
MD.Opt.StartDIIS            5
MD.maxIter                  1000        # default=1
MD.TimeStep                 0.5         # default=0.5 (fs)
MD.Opt.criterion            0.001       # default=1.0e-4 (Hartree/bohr)

<MD.Fixed.XYZ
      1   0 0 0
      2   0 0 0
      3   0 0 0
[...]
    482   0 0 0
    483   1 1 1
    484   1 1 1
[...]
    768   1 1 1
    769   1 1 1
    770   1 1 1
MD.Fixed.XYZ>

# MO output
```

```
MO.fileout                  off         # on|off

# DOS and PDOS
Dos.fileout                 off         # on|off, default=off
```

### B.1.2 Pt Nanomesh

```
#
#      File Name
#

System.CurrrentDirectory          ./    # default=./
System.Name                      ptbn_on
level.of.stdout                   1     # default=1 (1-3)
level.of.fileout                  1     # default=1 (0-2)

#
# Definition of Atomic Species
#

Species.Number       3
<Definition.of.Atomic.Species
 Pt    Pt6.0-s2p2d1    Pt_PBE
 B     B5.0-s2p2       B_PBE
 N     N4.0-s2p2       N_PBE
Definition.of.Atomic.Species>

#
# Atoms
#

Atoms.Number         443
Atoms.SpeciesAndCoordinates.Unit   Ang # Ang|AU


Atoms.UnitVectors.Unit              Ang #  Ang|AU
<Atoms.UnitVectors                      # unit=Ang.
   21.6614367967  -12.5062363657    0.0000000000
    0.0000000000   25.0124727313    0.0000000000
    0.0000000000    0.0000000000   50.0000000000
Atoms.UnitVectors>
```

```
<Atoms.SpeciesAndCoordinates           # Unit=Ang.
      1  Pt    0.802280    1.389580    0.000000    9.0  9.0
      2  Pt    0.802280    4.168750    0.000000    9.0  9.0
      3  Pt    0.802280    6.947910    0.000000    9.0  9.0
[...]
    243  Pt   -2.406830   -1.389580    4.538360    9.0  9.0
    244   N    0.019310   -0.005190    7.258610    2.5  2.5
    245   N    0.025380    2.511880    7.157980    2.5  2.5
[...]
    343   N   -2.167230   -1.263030    7.094930    2.5  2.5
    344   B    0.751720    1.250980    7.229610    1.5  1.5
    345   B    0.758270    3.785040    7.164530    1.5  1.5
[...]
    441   B   -1.433750   -5.083000    6.753880    1.5  1.5
    442   B   -1.441440   -2.517840    6.924600    1.5  1.5
    443   B   -1.428630   -0.002480    7.156780    1.5  1.5
Atoms.SpeciesAndCoordinates>

#
# SCF or Electronic System
#

scf.XcType                 GGA-PBE     # LDA|LSDA-CA|LSDA-PW|GGA-PBE
scf.SpinPolarization       Off         # On|Off|NC
scf.partialCoreCorrection  Off         # On|Off
scf.ElectronicTemperature  2500.0      # default=300 (K)
scf.energycutoff           200         # (Ry)
scf.maxIter                2000        # default=40
scf.EigenvalueSolver       Krylov      # DC|GDC|Cluster|Band
scf.Kgrid                  1 1 1       # means 4x4x4
scf.Mixing.Type            Kerker      # Rmm-Diisk
scf.Init.Mixing.Weight     0.0080      # default=0.30
scf.Min.Mixing.Weight      0.0010      # default=0.001
scf.Max.Mixing.Weight      0.0600      # default=0.40
scf.Mixing.History         5           # default=5
scf.Mixing.StartPulay      6           # default=6
scf.Kerker.factor          0.7         # default=1.0
scf.criterion              1.0e-3      # default=1.0e-6 (Hartree)

#
```

```
# 1D FFT
#

1DFFT.NumGridK              900         # default=900
1DFFT.NumGridR              900         # default=900
1DFFT.EnergyCutoff          3000
#
# Orbital Optimization
#

orbitalOpt.Method           Off         # Off|Unrestricted|Restricted
orbitalOpt.InitCoes     Symmetrical     # Symmetrical|Free
orbitalOpt.initPrefactor    0.1         # default=0.1
orbitalOpt.scf.maxIter      12          # default=12
orbitalOpt.MD.maxIter       5           # default=5
orbitalOpt.per.MDIter       100         # default=1000000
orbitalOpt.criterion        1.0e-4      # default=1.0e-4 (Hartree/borh)^2

#
# output of contracted orbitals
#

CntOrb.fileout              off         # on|off, default=off
Num.CntOrb.Atoms            1           # default=1
<Atoms.Cont.Orbitals
 1
Atoms.Cont.Orbitals>

#
# SCF Order-N
#

orderN.HoppingRanges        15.0        # default=5.0 (Ang)
orderN.NumHoppings          2           # default=2

#
# MD or Geometry Optimization
#

MD.Type                     EF          # Nomd|Opt|NVE|NVT_VS|NVT_NH
MD.Fixed.XYZ                On
```

```
#MD.Opt.DIIS.History       3
#MD.Opt.StartDIIS          5
MD.maxIter                 50          # default=1
MD.TimeStep                0.5         # default=0.5 (fs)
MD.Opt.criterion           0.001       # default=1.0e-4 (Hartree/bohr)


<MD.Fixed.XYZ
      1   1 1 1
      2   1 1 1
      3   1 1 1
[...]
    162   1 1 1
    163   0 0 0
    164   0 0 0
[...]
    441   0 0 0
    442   0 0 0
    443   0 0 0
MD.Fixed.XYZ>


#
# MO output
#

MO.fileout                 off         # on|off

#
# DOS and PDOS
#

Dos.fileout                off         # on|off, default=off
```

# Bibliography

[1] S. Cottenier. *Density Functional Theory and the family of (L)APW-methods: a step-by-step introduction* (Instituut voor Kern- en Stralingsfysica, K.U. Leuven, Belgium, 2002). URL `http://www.wien2k.at/reg_user/textbooks`.

[2] A. Nagashima, N. Tejima, Y. Gamou, T. Kawai, and C. Oshima. Electronic structure of monolayer hexagonal boron nitride physisorbed on metal surfaces. *Phys. Rev. Lett.* **75**, 3918 – 3921 (1995).

[3] A. B. Preobrajenski, A. S. Vinogradov, and N. Martensson. Ni 3d-BN $\pi$ hybridization at the h-BN/Ni(111) interface observed with core-level spectroscopies. *Physical Review B* **70**, 165404 (2004).

[4] G. B. Grad, P. Blaha, and K. Schwarz. Density functional thoery investigation of the geometric and spintronic structure of h-BN/Ni(111) in view of photoemission and STM experiments. *Physical Review B* **68**, 085404 (2003).

[5] M. Corso, W. Auwärter, M. Muntwiler, A. Tamai, Th. Greber, and J. Osterwalder. Boron nitride nanomesh. *Science* **303**, 217–220 (2004).

[6] S. Berner, M. Corso, R. Widmer, O. Groening, R. Laskowski, P. Blaha, K. Schwarz, A. Goriachko, H. Over, S. Gsell, M. Schreck, H. Sachdev,

T. Greber, and J. Osterwalder. Boron Nitride Nanomesh: Functionality from a corrugated monolayer. *Angew. Chem.-Int. Edit.* **46**, 5115 – 5119 (2007).

[7] R. Laskowski, P. Blaha, Th. Gallauner, and K. Schwarz. Single-layer model of the hexagonal boron nitride nanomesh on the Rh(111) surface. *Phys. Rev. Lett.* **98**, 106802 (2007).

[8] T. Ozaki. OpenMX. URL `http://www.openmx-square.org`.

[9] B. Aradi and Th. Frauenheim. DFTB - Density Functional based Tight Binding. URL `http://www.dftb.org`.

[10] E. Artacho, J. Gale, A. García, J. Junquera, R.M. Martin, P. Ordeón, D. Sánches-Portal, and J.M. Soler. SIESTA - Spanish Initiative for Electronic Simulations with Thousands of Atoms. URL `http://www.uam.es/departamentos/ciencias/fismateriac/siesta/`.

[11] P. Blaha, K. Schwarz, G. Madsen, D. Kvasnicka, and J. Luitz. *WIEN2k - An Augmented Plane Wave + Local Orbitals Program for Calculating Crystal Properties* (Univ. Prof. Dr. Karlheinz Schwarz, Vienna University of Technology, Institute of Materials Chemistry, Getreidemarkt 9/165, A-1060 Vienna/Austria, 2008). URL `http://www.wien2k.at`.

[12] P. Hohenberg and W. Kohn. Inhomogeneous electron gas. *Phys. Rev.* **136**, B864 (1964).

[13] W. Kohn and L.J. Sham. Self-consistent equations including exchange and correlation effects. *Phys. Rev.* **140**, A1133 (1965).

[14] J.P. Perdew and Y. Wang. Accurate and simple analytic representation of the electron-gas correlation energy. *Phys. Rev. B* **45**, 13244 (1992).

[15] J.P. Perdew, K. Burke, and M. Ernzerhof. Generalized gradient approximation made simple. *Phys. Rev. Lett.* **77**, 3865 – 3868 (1996).

[16] Georg K. H. Madsen, Peter Blaha, Karlheinz Schwarz, Elisabeth Sjöstedt, and Lars Nordström. Efficient linearization of the augmented plane-wave method. *Phys. Rev. B* **64**, 195134 (2001).

[17] J.C. Slater. Wave functions in a periodic potential. *Phys. Rev.* **51**, 846 (1937).

[18] O.K. Andersen. Linear methods in band theory. *Phys. Rev. B* **12**, 3060 (1975).

[19] T. Ozaki and H. Kino. Numerical atomic basis orbitals from H to Kr. *Phys. Rev. B* **69**, 195113 (2004).

[20] T. Ozaki. *Total energy and forces: Ver. 1.0* (2007). URL `http://www.openmx-square.org/tech_notes/tech1-1_0.pdf`.

[21] T. Ozaki and H. Kino. Efficient projector expanison for the *ab initio* LCAO method. *Phys. Rev. B* **72**, 045121 (2005).

[22] T. Ozaki. O(N) Krylov-subspace maethod for large-scale *ab initio* electronic structure calculations. *Phys. Rev. B* **74**, 245101 (2006).

[23] W. Yang. Direct calculation of electron density in density-functional theory. *Phys. Rev. Lett.* **66**, 1438 (1991).

[24] W. Yang and T. Lee. A density-matrix divide-and-conquer approach for electronic structure calculations of large molecules. *J. Chem. Phys.* **103**, 5674 (1995).

[25] R. Haydock, V. Heine, and M.J. Kelly. Electronic structure based on the local atomic environment for tight-binding bands. *J. Phys. C* **5**, 2845 (1972).

[26] D. G. Pettifor. New many-body potential for the bond order. *Phys. Rev. Lett.* **63**, 2480 (1989).

[27] M. Aoki. Rapidly convergent bond order expansion for atomistic simulations. *Phys. Rev. Lett.* **71**, 3842 (1993).

[28] A.P. Horsfield, A.M. Bratkovsky, D.G. Pettifor, and M. Aoki. Bond-order potential and cluster recursion for the description of chemical bonds: Efficeint real-space methods for tight-binding molecular dynamics. *Phys. Rev. B* **53**, 1656 (1996).

[29] T. Ozaki and K. Terakura. Convergent recursive O(N) method for ab initio tight-binding calculations. *Phys. Rev. B* **64**, 195126 (2001).

[30] T. Ozaki. Bond-order potential based on the Lanczos basis. *Phys. Rev. B* **59**, 16061 (1999).

[31] C. Lanczos. An iteration method for the solution of the eigenvalue problem of linear differential and integral operators. *J. Res. Nat. Stand.* **45**, 255 – 281 (1950).

[32] S. Ismail-Beigi and T. Arias. Locality of the density matrix in metals, semiconductors, and insulators. *Phys. Rev. Lett.* **82**, 2127 (1999).

[33] Ph. Mavropoulos and N. Papaniklaou. The Korringa-Kohn-Rostoker (KKR) Green function method. *NIC Series* **31**, 131 – 158 (2006).

[34] J. Khandogin, K. Musier-Forsyth, and D.M. York. Insights into the regioselectivity and RNA-binding affinity of HIV-1 nucleocapsid protein from linear-scaling quantum methdos. *J. Mol. Biol.* **330**, 993 (2003).

[35] T. Ozaki. *Geometry Optimization: Ver. 1.0* (2007). URL `http://www.openmx-square.org/tech_notes/tech7-1_0.pdf`.

[36] P. Csaszar and P. Pulay. Geometry optimization by DIIS. *J. Mol. Struct.* **114**, 31 (1984).

[37] F. Eckert, P. Pulay, and H.J. Werner. Ab initio geometry optimization for large molecules. *J. Comp. Chem.* **18**, 1473 (1997).

[38] C.G. Broyden. The convergence of a class of double-rank minimization algorithms. *J. Inst. Math. Appl.* **6**, 76 (1970).

[39] R. Fletcher. A new approach to variable metric algorithms. *Comput. J.* **13**, 317 (1970).

[40] D. Goldfarb. A family of variable metric methods derived by variational means. *Math. Comp.* **24**, 23 (1970).

[41] D.F. Shanno. Conditioning of Quasi-Newton methods for function minimization. *Math. Comp.* **24**, 647 (1970).

[42] A. Banerjee, N. Adams, J. Simons, and R. Shepard. Search for stationary points on surfaces. *J. Phys. Chem.* **89**, 52 – 57 (1985).

[43] U. von Barth and G. Grossmann. Dynamical effects in X-ray spectra and the final-state rule. *Physical Review B* **25**, 5150–5179 (1982).

[44] A. R. Williams and R. A. deGroot. Generalization of Slater's stransition state concept. *J. Chem. Phys.* **63**, 628 – 631 (1975).

[45] J. P. Perdew and A. Zunger. Self-interaction correction to density-functional approximations for many-electron systems. *Phys. Rev. B* **23**, 5048 – 5079 (1981).

[46] P. Reza, J. Bruleyb, P. Brohanc, M. Paynec, and L.A.J. Garvie. Review of methods for calculating near edge structure. *Ultramicroscopy* **59**, 159 (1995).

[47] W. Auwärter, T.J. Kreutz, T. Greber, and J. Osterwalder. XPD and STM investigation of hexagonal boron nitride on Ni(111). *Surf. Sci.* **429**, 229–236 (1999).

[48] M. Muntwiler, W. Auwärter, F. Baumberger, M. Hoesch, T. Greber, and J. Osterwalder. Determining adsorbate structures from substrate emission X-ray photoelectron diffraction. *Surf. Sci.* **472**, 125 (2001).

[49] C. Oshima and A. Nagashima. Ultra-thin epitaxial films of graphite and hexagonal boron nitride on solid surfaces. *J. Phys.: Condens. Matter* **9**, 1 (1997).

[50] E. Rokuta, Y. Hasegawa, K. Suzuki, Y. Gamou, C. Oshima, and A. Nagashima. Phonon dispersion of an epitaxial monolayer film of hexagonal boron nitride on Ni(111). *Phys. Rev. Lett.* **79**, 4609 (1997).

[51] D. A. Liberman. Slater transition-state band-structure calculations. *Phys. Rev. B* **62**, 6851 – 6853 (2000).

[52] I. Shimoyama, Y. Baba, T. Sekiguchi, and K.G. Nath. NEXAFS spectra of an epitaxial boron nitride film on Ni(111). *J. El. Spec.* **137**, 573–578 (2004).

[53] P. Widmayer, H.-G. Boyen, P. Ziemann, P. Reinke, and P. Oelhafen. Electron spectroscopy on boron nitride thin films: Comparison of near-surface to bulk electronic properties. *Phys. Rev. B* **59**, 5233 (1999).

[54] G. G. Fuentes, E. Borowiak-Palen, T. Pichler, X. Liu, A. Graff, G. Behr, R. J. Kalenczuk, M. Knupfer, and J. Fink. Electronic structure of multiwall boron nitride nanotubes. *Phys. Rev. B* **67**, 035429 (2003).

[55] R. F. Pettifer, C. Brouder, M. Benfatto, C. R. Natoli, C. Hermes, and M. F. Ruiz Lopez. Magic-angle theorem in powder X-ray-absorption spectroscopy. *Phys. Rev. B* **42**, 37 – 42 (1990).

[56] L. J. Terminello, A. Chaiken, D. A. Lapiano-Smith, G. L. Doll, and T. Sato. Morphology and bonding measured from boron-nitride powders and films using near-edge X-ray absorption fine structure. *J. Vac. Sci. Technol. A* **12**, 2462 (1994).

[57] D. Li, G. M. Bancroft, and M. E. Fleet. B K-edge XANES of crystalline and amorphous inorganic materials. *J. Electron Spectrosc. Relat. Phenom.* **79**, 71 (1996).

[58] R. Franke, S. Bender, J. Hormes, A. A. Pavlychev, and N.G. Fominych. A quasi-atomic treatment of chemical and structural effects on K-shell excitations in hexagonal and cubic BN crystals. *Chem. Phys.* **216**, 243 (1997).

[59] J. Barth, C. Kunz, and T.M. Zimkina. Photoemission investigation of hexagonal BN: band structure and atomic effects. *Solid State Commun.* **36**, 453 (1980).

[60] T. Ozaki. Linear scaling Krylov subspace method for large scale *ab initio* electronic structure calculations of metals. *arXiv:cond-mat* 0509291v1 (2005).

[61] R. Takayama, T. Hoshi, and T. Fujiwara. Krylov subspace method for molecular dynamics simulation based on large-scale electronic structure theory. *J. Pyhs. Soc. Jpn.* **73**, 1519 – 1524 (2004).

[62] G.P. Kerker. Efficient iteration scheme for self-consistent pseudopotential calculations. *Phys. Rev. B* **23**, 3082 – 3084 (1981).

[63] T. Ozaki. Variationally optimized atomic orbitals for large-scale electronic structures. *Phys. Rev. B* **67**, 155108 (2003).

[64] R. Laskowski and P. Blaha. Unravling the structure of the h-BN/Rh(111) nanomesh with *ab initio* calculations. *J. Phys. Cond. Matter* **20**, 064207 (2008).

[65] R. Laskowski and P. Blaha. *Ab initio* study of *h*-BN nanomeshes on Ru(001), Rh(111), and Pt(111). *Phys. Rev. B* **81**, 075418 (2010).

[66] Z. Wu and R.E. Cohen. More accurate generalized gradient approximation for solids. *Phys. Rev. B* **73**, 235116 (2006).

[67] A.B. Preobrajenski, A.S. Vinogradov, May Ling Ng, E. Ćavar, R. Westerström, A. Mikkelsen, E. Lundgren, and N. Mårtensson. Influence of chemical interaction at the lattice-mismatched h-BN/Rh(111) and h-BN/Pt(111) interfaces on the overlayer morphology. *Phys. Rev. B* **75**, 245412 (2007).

[68] NIST. URL `http://physics.nist.gov/PhysRefData/DFTdata/contents.html`.

# List of Figures

# List of Tables